

FY21 Progress Report on BISON Metallic Fuel Model Development and V&V Using EBR-II Legacy Data

Evaluation of the BISON code for simulating metallic fuels under steady-state fast reactor conditions

Chemical & Fuel Cycle Technologies Division

About Argonne National Laboratory

Argonne is a U.S. Department of Energy laboratory managed by UChicago Argonne, LLC under contract DE-AC02-06CH11357. The Laboratory's main facility is outside Chicago, at 9700 South Cass Avenue, Argonne, Illinois 60439. For information about Argonne and its pioneering science and technology programs, see www.anl.gov.

DOCUMENT AVAILABILITY

Online Access: U.S. Department of Energy (DOE) reports produced after 1991 and a growing number of pre-1991 documents are available free at OSTI.GOV (<http://www.osti.gov/>), a service of the US Dept. of Energy's Office of Scientific and Technical Information.

Reports not in digital format may be purchased by the public from the National Technical Information Service (NTIS):

U.S. Department of Commerce
National Technical Information Service
5301 Shawnee Rd
Alexandria, VA 22312
www.ntis.gov
Phone: (800) 553-NTIS (6847) or (703) 605-6000
Fax: (703) 605-6900
Email: **orders@ntis.gov**

Reports not in digital format are available to DOE and DOE contractors from the Office of Scientific and Technical Information (OSTI):

U.S. Department of Energy
Office of Scientific and Technical Information
P.O. Box 62
Oak Ridge, TN 37831-0062
www.osti.gov
Phone: (865) 576-8401
Fax: (865) 576-5728

Disclaimer

This report was prepared as an account of work sponsored by an agency of the United States Government. Neither the United States Government nor any agency thereof, nor UChicago Argonne, LLC, nor any of their employees or officers, makes any warranty, express or implied, or assumes any legal liability or responsibility for the accuracy, completeness, or usefulness of any information, apparatus, product, or process disclosed, or represents that its use would not infringe privately owned rights. Reference herein to any specific commercial product, process, or service by trade name, trademark, manufacturer, or otherwise, does not necessarily constitute or imply its endorsement, recommendation, or favoring by the United States Government or any agency thereof. The views and opinions of document authors expressed herein do not necessarily state or reflect those of the United States Government or any agency thereof, Argonne National Laboratory, or UChicago Argonne, LLC.

FY21 Progress Report on BISON Metallic Fuel Model Development and V&V Using EBR-II Legacy Data

Evaluation of the BISON code for simulating metallic fuels under steady-state fast reactor conditions

prepared by
Yinbin Miao, Aaron Oaks, and Abdellatif M. Yacout
Chemical & Fuel Cycle Technologies Division, Argonne National Laboratory

Christopher Matthews
Los Alamos National Laboratory

Stephen Novascone
Idaho National Laboratory

prepared for
U.S. Department of Energy
Nuclear Energy Advanced Modeling & Simulation Program

September 30, 2021

EXECUTIVE ABSTRACT

In this report, the activities and achievements made by Argonne National Laboratory for the Nuclear Energy Advanced Modeling and Simulation (NEAMS) BISON code metallic fuel validation and verification project in FY2021 are summarized. The cladding degradation model based on the FCCI/CCCI wastage calculations has been developed and implemented into BISON. A comprehensive evaluation of the cladding degradation model was performed based on FIPD data of the IFR experiment X447. BISON objects were also developed to enable direct use of time-varying cladding outer surface temperature profile as temperature boundary conditions, which proved to provide more accurate temperature predictions for the metallic fuel pins irradiated in EBR-II. Additionally, a new BISON object was implemented to enable direct comparison between BISON predicted data and FIPD-based post-irradiation examination (PIE) results, which would significantly facilitate BISON metallic fuel verification and validation (V&V) activities. These new BISON-FIPD integration features were used in the establishment of a low-burnup fuel swelling evaluation framework as demonstration. The framework was successfully used to evaluate current fuel swelling models based on the IFR experiment X423.

ACKNOWLEDGEMENT

This work was funded by the U.S. Department of Energy (DOE)'s Nuclear Energy Advanced Modeling and Simulation (NEAMS) program. The efforts involving Argonne National Laboratory were supported under Contract No. DE-AC02-06CH11357 between UChicago Argonne, LLC and the U.S. Department of Energy.

Table of Contents

EXECUTIVE ABSTRACT.....	I
ACKNOWLEDGEMENT.....	II
TABLE OF CONTENTS.....	III
LIST OF FIGURES	IV
LIST OF TABLES	VI
1 INTRODUCTION	1
2 CLADDING DEGRADATION MODEL DEVELOPMENT	2
1.1 BRIEF REVIEW OF FCCI AND CCCI MODELS.....	2
1.2 INTRODUCTION OF DEGRADATION FACTOR	3
1.3 IMPLEMENTATION INTO BISON	6
1.4 BISON CLADDING DEGRADATION MODEL EVALUATION	7
1.4.1 BISON-FIPD INTEGRATION AND X447/A EXPERIMENT	7
1.4.2 EVALUATION RESULTS AND DISCUSSION	11
1.4.2.1 BISON CALCULATED CONDITION PARAMETERS	11
1.4.2.2 BISON PREDICTED FCCI/CCCI WASTAGE.....	14
1.4.2.3 CLADDING DEGRADATION AND DEFORMATION.....	15
1.4.2.4 GUIDANCE FOR FUTURE IMPROVEMENTS.....	21
3 FIPD-INFORMED TEMPERATURE BOUNDARY CONDITIONS	22
1.5 DEVELOPMENT OF TIME-VARYING TEMPERATURE IN FIPD	22
1.6 UTILIZATION OF THE TIME-VARYING TEMPERATURE IN BISON	24
1.7 ADVANTAGES OF THE NEW APPROACH	26
4 ASSESSMENT OF LOW-BURNUP SWELLING.....	29
1.8 BRIEF REVIEW OF INVESTIGATED BISON SWELLING MODEL	29
1.9 IFR IRRADIATION EXPERIMENT X423 IN FIPD.....	30
1.9.1 BRIEF INTRODUCTION OF THE X423 EXPERIMENT	30
1.9.2 LEVERAGING BISON-FIPD INTEGRATION	31
1.9.2.1 IRRADIATION CONDITION PARAMETERS IN FIPD.....	31
1.9.2.2 POST-IRRADIATION EXAMINATION RESULTS IN FIPD	31
1.9.2.3 DEVELOPMENT OF BISON OBJECT TO FACILITATE PIE-PREDICTION COMPARISON.....	32
1.10 ASSESSMENT RESULTS	33
5 CONCLUSIONS AND FUTURE PLANS.....	39
5.1 CONCLUSIONS.....	39
5.2 FUTURE PLANS.....	39
REFERENCES	41

LIST OF FIGURES

Figure 2-1 A metallograph of sectioned DP04 irradiated in X447/A showing the FCCI and CCCI wastage layers.	2
Figure 2-2 A schematic drawing showing the definition of degradation factors.	4
Figure 2-3 Temperature and fast neutron flux profile used for sensitivity test.	5
Figure 2-4 Sensitivity study of the degradation factor selection. The relative differences shown here are between a reduced-thickness cladding mesh (reference) and the original-thickness cladding mesh with degradation factor in the wastage layer.	6
Figure 2-5 A flow chart of how the FCCI/CCCI related modules are coupled with other BISON fuel performance modules.	6
Figure 2-6 A brief schematic showing the U-10Zr/HT9 pins locations in X447/A subassembly.	8
Figure 2-7 Typical FIPD-based input data used for BISON simulation focused on FCCI/CCCI.	9
Figure 2-8 Pin-by-pin maximum peak linear power and fast neutron flux of the U-10Zr/HT9 pins in X447/A Subassembly.	10
Figure 2-9 Pin-by-pin maximum burnup of the U-10Zr/HT9 pins in X447/A Subassembly..	11
Figure 2-10 Comparison between BISON-predicted peak cladding temperatures and FIPD-recorded peak cladding temperatures indicating the limitations of current BISON coolant channel model.	12
Figure 2-11 Time-evolution of peak cladding temperature for four representative pins.	13
Figure 2-12 Fission gas release (FGR) data predicted by the BISON code for the four representative pins irradiated in X447/A subassembly: (a) time evolution of fractional fission gas release using BISON's generic coolant channel; (b) time evolution of plenum pressure using BISON's generic coolant channel; (c) time evolution of fractional fission gas release using BISON's sodium coolant channel; (d) time evolution of plenum pressure using BISON's sodium coolant channel. Note that the FGR behaviors predicted by the two coolant channel models are similar because the FGR is less sensitive to temperature compared to other behaviors such as FCCI/CCCI.	14
Figure 2-13 FCCI and CCCI wastage thickness of 15 HT9 clad pins irradiated in both X447 and X447A subassemblies: (a) FCCI wastage predicted by BISON using both BISON's generic and sodium coolant channel (GCC/SCC) models compared to PIE data [19]; (b) CCCI wastage predicted by BISON using both BISON's generic and sodium coolant channel (GCC/SCC) models with measured CCCI wastage thickness from DP04. Note that the measured CCCI thickness only contains carbon depletion layer (d_{cd}) and is thus lower than both BISON predicted values.	15
Figure 2-14 Maximum CDF of all HT9 clad fuel pins irradiated in X447 and X447A subassemblies predicted by BISON using both generic and sodium coolant channel models.	16
Figure 2-15 Comparison between BISON predicted CDF and observed failed pins during X447/A experiment: (a) BISON predicted CDF ranges and corresponding failure probability based on the correlation described in Ref. [31]; (b) Probabilities of observing a specified number of failed pins predicted by BISON using the two coolant channel models.	17
Figure 2-16 BISON predicted cladding deformation of four representative HT9 clad fuel pins irradiated in X447/A subassembly compared with PIE data [19], [32].	18

Figure 2-17 Statistical fuel cladding outer diameters of all 15 HT9 clad fuel pins irradiated in both X447 and X447A subassemblies: (a) a diagram showing the three different categories of HT9 clad pins: inner (located near the subassembly center), outer (located near the dummy pins), and replaced (replaced with fresh pins during reconstitution); (b) range of predicted cladding deformation using generic coolant channel model; (c) range of predicted cladding deformation using sodium coolant channel.....	20
Figure 3-1 Overview of the computer codes and data used to calculate the operating parameters presented in FIPD [18].	22
Figure 3-2 Time-dependent peak cladding temperature in FIPD.....	23
Figure 3-3 Maximum cladding temperature at different axial positions.....	24
Figure 3-4 a schematic drawing showing different options in FIPDAxialProfileFunction to process values beyond fuel end positions.	25
Figure 3-5 Maximum FCCI wastage thickness of X447A pins as predicted by BISON using the FIPD-based temperature BC in comparison with the results using BISON’s generic and sodium coolant channel models.	27
Figure 3-6 Pin-by-pin logarithmic CDF as predicted by BISON using the FIPD-based temperature BC.	27
Figure 3-7 The probability of observing a specific number of failed pin as predicted by BISON using different temperature BCs.	28
Figure 4-1 Summary of time-and-radial averaged axial fuel temperature range and burnup range of fuel pins with different Pu loading values that were irradiated and examined in the IFR experiment X423.....	30
Figure 4-2 Procedures used to extract fuel radial and axial swelling strain from thermal neutron NRAD images.	32
Figure 4-3 Differences between BISON predicted fuel radii using the two current swelling models and NRAD measured fuel radii as a function of burnup.	34
Figure 4-4 Comparison between BISON predicted fuel radius and NRAD measured fuel radius for a typical U-10Zr pin.....	35
Figure 4-5 Comparison between BISON predicted fuel radius and NRAD measured fuel radius for a typical U-3Pu-10Zr pin.	36
Figure 4-6 Comparison between BISON predicted fuel radius and NRAD measured fuel radius for a typical U-8Pu-10Zr pin.	36
Figure 4-7 Comparison between BISON predicted fuel radius and NRAD measured fuel radius for a typical U-19Pu-10Zr pin.	37
Figure 4-8 Comparison between BISON predicted fuel radius and NRAD measured fuel radius for a typical U-22Pu-10Zr pin.	37
Figure 4-9 Comparison between BISON predicted fuel radius and NRAD measured fuel radius for a typical U-26Pu-10Zr pin.	38

LIST OF TABLES

Table 4-1 FIPD-based input data used in the low-burnup swelling evaluation framework.....	31
---	----

1 Introduction

Advanced fast neutron reactors are attractive to the nuclear power industry for their unique features such as achievement of ultra-high burnup and transmutation of actinides [1]. Based on the abundant experience accumulated within the Integral Fast Reactor (IFR) program [2], metallic fuels, U-10Zr and U-Pu-10Zr contained by stainless-steel cladding, have been regarded as the main fuel choices of the U.S. advanced fast neutron reactors [3]–[7]. In order to support the development, qualification, and licensing of these advanced fast reactors, the performance of metallic fuels must be predicted with high fidelity using advanced fuel performance codes such as BISON [8].

BISON is an advanced engineering-scale fuel performance code based on multiphysics finite element method (FEM) simulations enabled by the MOOSE framework [9]. As a general fuel performance code, BISON has modules that can be used for performance simulations of a variety of fuel and reactor types, including the conventional UO₂-Zr-based fuel-cladding solution [10] and enhanced accident tolerance fuel (EATF) solutions [11] for light water reactors (LWRs), TRISO fuel for gas-cooled reactors and micro-reactors [12], and metallic [13]–[15] and MOX fuel [16] for sodium-cooled fast reactors (SFRs). Supported by the Nuclear Energy Advanced Modeling and Simulation (NEAMS) Program, efforts have been made to enhance the capabilities of the BISON code in simulating metallic fast reactor fuels, which include the implementation of both the descriptive models that were deduced using legacy experimental data and the predictive models based on physical mechanisms and informed by lower-length-scale (LLS) simulations. Meanwhile, the verification and validation (V&V) of the BISON metallic fuel models will rely on abundant legacy data from the IFR program, many of which are preserved and maintained in the EBR-II Fuel Irradiation & Physics Database (FIPD) [17], [18]. As part of the BISON metallic fuel team, the Argonne National Laboratory (ANL) team have been contributing to both model development/implementation and V&V work. In FY2021, three major achievements were made: (1) A cladding degradation model based on wastage formation on both cladding surfaces was implemented and evaluated using BISON-FIPD integration tools; (2) the FIPD-based time-varying temperature boundary condition feature was implemented in BISON and demonstrated using X447 data; and (3) the FIPD axial post-irradiation examination (PIE) data comparison object was implemented into BISON and utilized with other BISON-FIPD integration tools to establish a framework to assess low-burnup fuel swelling models. These FY2021 achievements are reported in detail here.

2 Cladding Degradation Model Development

Cladding degradation due to fuel-cladding chemical interaction (FCCI) and coolant-cladding chemical interaction (CCCI) is one of the major mechanisms of cladding failure for metallic fuels. For HT9 clad metallic fuel, FCCI/CCCI-based cladding degradation is responsible for the only experimentally observed cladding failures, which were observed in the IFR X447 experiment [19]. In this chapter, the implementation of empirical FCCI/CCCI models performed previously is first reviewed. Then, the cladding mechanical degradation model development for BISON based on calculated FCCI/CCCI thickness is described. The performance of this new cladding degradation model is then evaluated using the IFR X447 experiment data as an example.

2.1 Brief Review of FCCI and CCCI Models

During reactor operation, chemical interaction happens on both inner (FCCI) and outer (CCCI) surfaces of the cladding, as shown in Figure 2-1. Both interaction mechanisms lead to loss of mechanical strength of the cladding material and thus reduce the effective cladding thickness. Thus, FCCI and CCCI are the two major causes of cladding degradation in metallic fast reactor fuels.

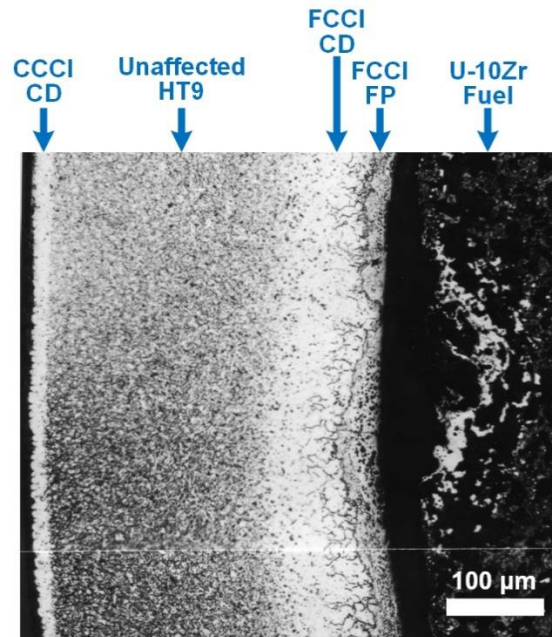


Figure 2-1 A metallograph of sectioned DP04 irradiated in X447/A showing the FCCI and CCCI wastage layers.

In FY2019 and FY2020, empirical correlations for both FCCI and CCCI of metallic fast reactor fuel were implemented into BISON as `MetallicFuelWastage` and `MetallicFuelCoolantWastage` objects. As multiple forms of correlations are available in BISON for different cladding materials (e.g., D9, SS316, and HT9), the users have options to select their preferred correlations. In this report, the burnup-dependent FCCI and temperature dependent CCCI correlations for HT9 cladding are focused for cladding degradation model evaluation. The detailed forms and parameters of the related FCCI and CCCI correlations can be found on BISON documentation website [20].

2.2 Introduction of Degradation Factor

The FCCI and CCCI correlations referred to in Section 1 merely calculate the thickness values of both interactions without taking their impact on cladding performance into account. In this section, the efforts of modeling cladding mechanical degradation based on calculated FCCI/CCCI wastage thickness are introduced.

It is worth mentioning here that both the implemented FCCI and CCCI correlations assume planar front movement as the cladding radius is much higher than the cladding thickness. However, the major effect of FCCI/CCCI in metallic fuel is inducing mechanical degradation into cladding. Therefore, the fraction of cladding that corresponds to the wastage thickness needs to be treated differently from the unaffected cladding material in BISON simulations. The most accurate approach to handle such shifts in material properties should be through extended finite element method (XFEM) [21]. However, XFEM is computationally expensive, and it is not ideal for engineering scale simulation over the entire lifetime of whole fuel pins. Hence, a simplified approach must be developed to enable mechanical degradation simulation of cladding affected by FCCI and CCCI with acceptable accuracy. In this study, a degradation factor, F_{degr} , is introduced to account for the effect of FCCI/CCCI formation on cladding mechanical properties. F_{degr} is set as F_{clad} (usually equal to 1) for the cladding elements that are free from FCCI/CCCI. Once the cladding elements are affected by FCCI/CCCI according to the calculated wastage thickness, F_{degr} is set as F_{wst} . Optionally, a sine function can be used to make a smooth transition between the affected and unaffected cladding elements. Thus, F_{degr} has the following expression:

$$F_{degr}(r) = \begin{cases} F_{wst,fcci} & r \in [r_i, r_1] \\ \frac{1}{2}(F_{clad} - F_{wst,fcci}) \left[1 + \sin\left(\frac{r-r_i-d_{fcci}}{w_{tr,fcci}}\pi\right) \right] + F_{wst,fcci} & r \in (r_1, r_2] \\ F_{clad} & r \in (r_2, r_3] \\ \frac{1}{2}(F_{clad} - F_{wst,ccci}) \left[1 + \sin\left(\frac{r-r_o+d_{fcci}}{w_{tr,ccci}}\pi\right) \right] + F_{wst,ccci} & r \in (r_3, r_4] \\ F_{wst,ccci} & r \in (r_4, r_o] \end{cases}; \quad (2-1)$$

$$\begin{cases} r_1 = r_i + d_{fcci} - 0.5w_{tr,fcci} \\ r_2 = r_i + d_{fcci} + 0.5w_{tr,fcci} \\ r_3 = r_o - d_{ccci} - 0.5w_{tr,fcci} \\ r_4 = r_o - d_{fcci} + 0.5w_{tr,fcci} \end{cases}. \quad (2-2)$$

Here, r_i and r_o are inner and outer radii of the cladding, respectively; d_{fcci} and d_{ccci} are thickness values of FCCI and CCCI wastage layers calculated by the corresponding BISON Materials objects, respectively; $w_{tr,fcci}$ and $w_{tr,ccci}$ are the transition widths of FCCI and CCCI wastage, respectively. The profile of $F_{degr}(r)$ is illustrated in Figure 2-2 to provide a more specific example. When the wastage thickness (d_i) is lower than half of the corresponding preset transition width ($w_{tr,i}$), $2d_i$ is used as transition width instead. All the geometry parameters are taken from the non-displaced mesh. This degradation factor was implemented into the BISON code as a Function object named `MetallicFuelWastageDegradationFunction`. The Function object gets FCCI and/or CCCI wastage thickness from `VectorPostprocessors` and calculates the degradation factor, F_{degr} , as a MOOSE Function.

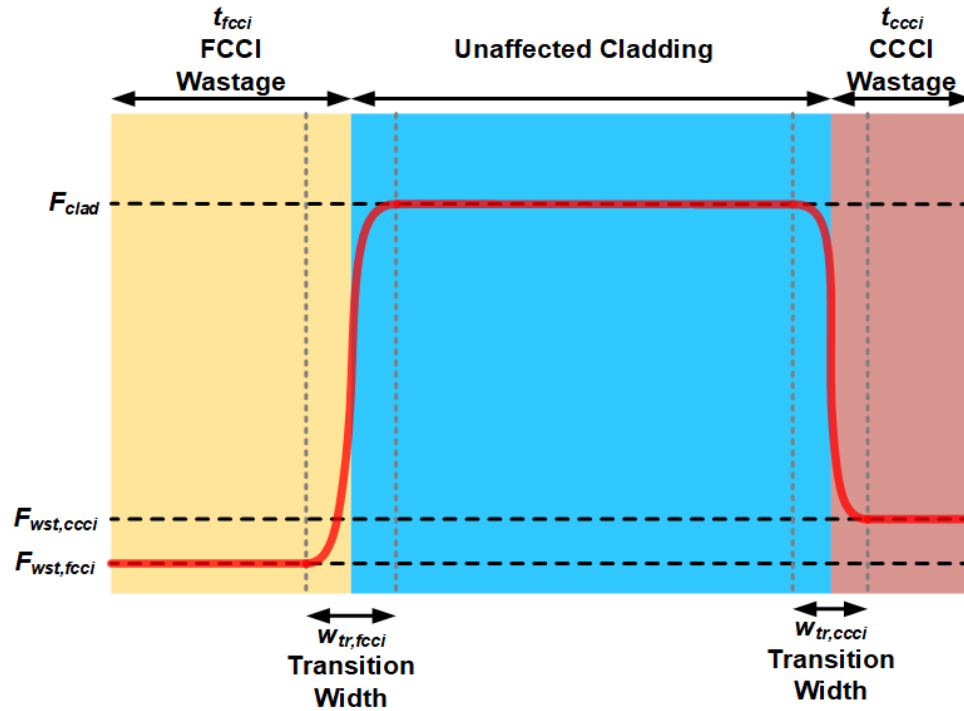


Figure 2-2 A schematic drawing showing the definition of degradation factors.

To induce the mechanical properties degradation, $F_{degr}(r)$ (the Function) was used to scale both elastic and plastic mechanical models in BISON. To be specific, the degradation factor was applied to the tensor elasticity and creep formulation models for each material (i.e., HT9, SS316, D9, etc.). The degradation factor is used to scale elastic moduli, whereas the reciprocal degradation factor is used to scale creep strain rate.

In this model, the key mechanical behavior of the degraded cladding is highly dependent on the selection of $F_{wst,fcci}$ and $F_{wst,ccci}$. In this study, it is assumed that the calculated wastage thickness does not contribute to the cladding mechanical strength. That is, the cladding with wastage layers on both surfaces is expected to have the same mechanical behavior as a reduced-thickness cladding that excludes the wastage layers. Hence, the ideal F_{wst} is zero. However, to ensure solver convergence, a sufficiently small but non-zero F_{wst} must be used. A sensitivity test was performed assuming $F_{wst,fcci} = F_{wst,ccci}$. In this test, an empty HT9 cladding with a height of 0.5 m, an inner diameter of 6 mm, and a wall thickness of 0.381 mm was simulated. The cladding was assumed to have a fixed FCCI wastage layer with 0.125 mm thickness and a CCCI wastage layer with 0.031 mm thickness. The axial cladding temperature and fast neutron flux profiles were set as cosine functions with peak values of 677 °C and $5.0 \times 10^{19} \text{ n/m}^2 \cdot \text{s}$ in the center (see Figure 2-3).

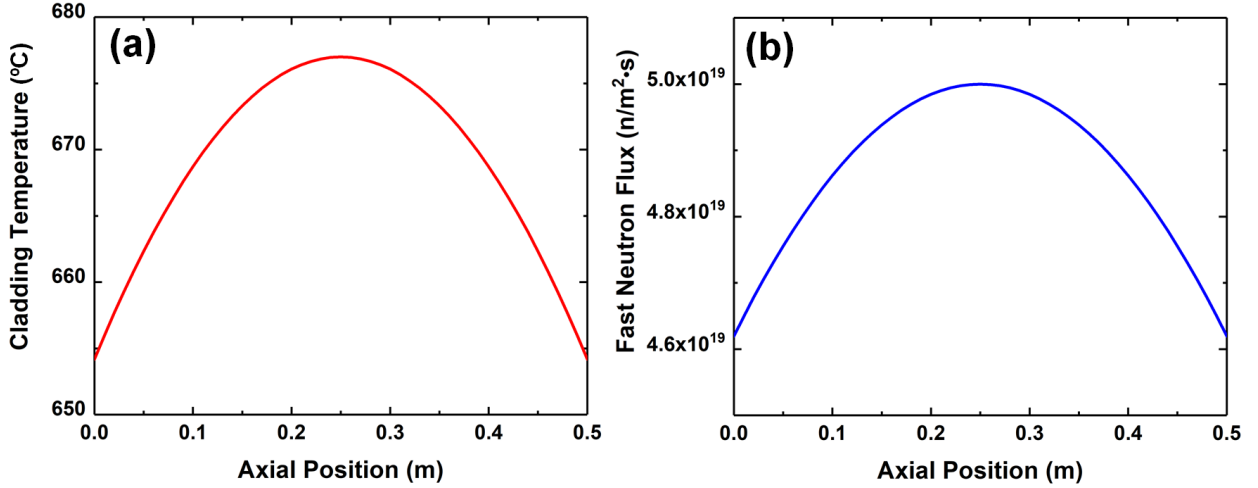


Figure 2-3 Temperature and fast neutron flux profile used for sensitivity test.

The simulation lasted for 1.8×10^6 s with the initial 1 MPa internal pressure linearly increased to 8.2 MPa with time. F_{wst} ranging from 0.0003 up to 1.0 was investigated focusing on its effect on maximum cladding deformation strain and cumulative damage fraction (CDF). Here, CDF is a measure of the cladding damage, which is defined as follows:

$$CDF = \int_0^t \frac{dt}{t_r(\sigma, T)}, \quad (2-3)$$

where $t_r(\sigma, T)$ is the experimentally measured creep-rupture time, which is a function of stress (σ) and temperature (T). CDF is a statistical tool to evaluate the lifetime of cladding. Meanwhile, cladding strain is the major cladding degradation quantity that can be directly measured during PIE. Hence, these two quantities were chosen as criteria for F_{wst} selection. Here, the optimized degradation factor (F_{wst}) was assumed to replicate the maximum cladding deformation and CDF values of a reference cladding with a reduced thickness (0.225 mm) by removing wastage layers from the mesh. The relative differences in maximum cladding deformation and CDF values between the degradation model and the reference reduced thickness model are shown in Figure 2-4. It is clear that F_{wst} of 0.001 is capable of predicting CDF and cladding deformation with differences less than 7% and 3%, respectively. On the other hand, a F_{wst} lower than 0.0005 frequently leads to solver convergence issue. This F_{wst} of 0.001 has been set as default value in the BISON object and was adopted in the rest of this paper.

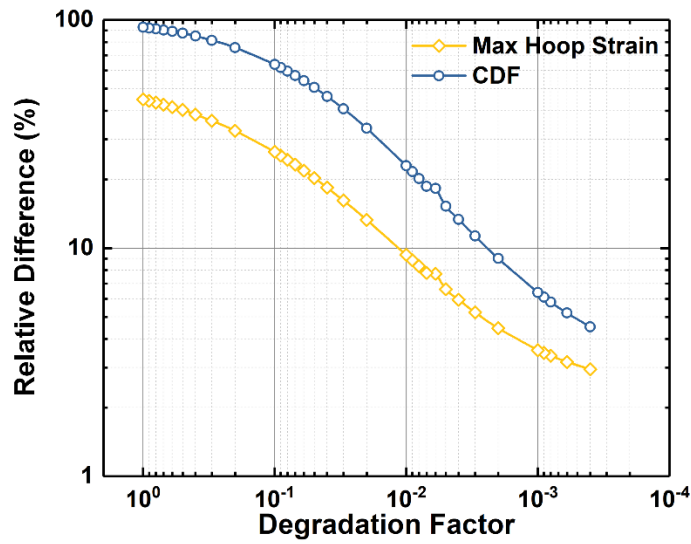


Figure 2-4 Sensitivity study of the degradation factor selection. The relative differences shown here are between a reduced-thickness cladding mesh (reference) and the original-thickness cladding mesh with degradation factor in the wastage layer.

2.3 Implementation into BISON

The cladding degradation model has been implemented into BISON as a Functions object named `MetallicFuelWastageDegradationFunction`. This object needs to work with other BISON objects to calculate the cladding degradation and apply it to mechanics models. A brief flow chart that describes the relation between this object and other BISON objects is shown as Figure 2-5.

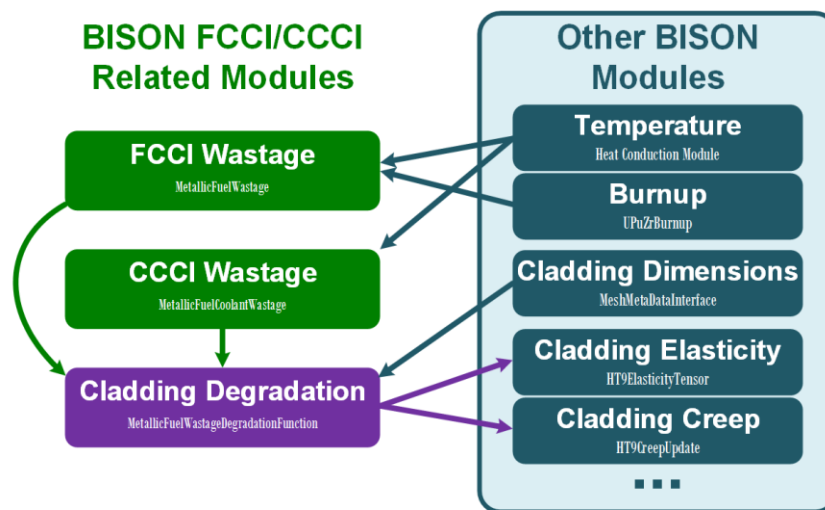


Figure 2-5 A flow chart of how the FCCI/CCCI related modules are coupled with other BISON fuel performance modules.

This `MetallicFuelWastageDegradationFunction` needs to get axially-dependent FCCI or CCCI information from the corresponding wastage calculation Materials objects (i.e., `MetallicFuelWastage` and `MetallicFuelCoolantWastage`). In addition, the fuel pin geometry parameters can be obtained from the FIPD-informed mesh generator through `MeshMetaDataInterface`. After calculating the cladding degradation factor, this value is transferred to the elasticity and creep modules of the cladding material in BISON. To be specific, the elastic modulus tensor (e.g., `HT9ElasticityTensor`) is scaled by the degradation factor to effectively soften the cladding materials. Meanwhile, the creep strain rate (e.g., `HT9CreepUpdate`) is scaled by the reciprocal degradation factor. Additionally, there are two coolant channel models available in BISON to calculate the sodium coolant temperature and heat transfer coefficient. One is based on BISON's generic coolant channel (GCC) model, which was originally developed for LWR applications and expanded to SFR applications by adopting sodium properties and hexagonal geometry; the other is a sodium coolant channel (SCC) model, which was recently developed specifically for SFR applications. The GCC model adopts the modified Schad correlation [22] to calculate the Nusselt number, while the SCC model predicts the Nusselt number using either the FFTF correlation [23] or the BGF correlation [24]. Both GCC and SCC (the BGF correlation) models were used in this study for comparison.

2.4 BISON Cladding Degradation Model Evaluation

In this section, the evaluation of the aforementioned metallic fuel cladding degradation modeling approach is evaluated using legacy in-pile irradiation data of the IFR program maintained in the FIPD database. This evaluation will leverage the frameworks built under the ongoing BISON-FIPD integration project.

2.4.1 BISON-FIPD Integration and X447/A Experiment

The IFR Experiment X447/A was selected to be used for evaluating the implemented FCCI/CCCI cladding degradation models in BISON. X447/A was designed to test the high-temperature performance of HT9 cladding and its compatibility with binary U-10Zr fuel. The experiment utilized MK-D61 inner blanket driver type subassembly hardware, which contained up to 61 fuel pins. The coolant was orificed in this experiment to intentionally raise peak HT9 cladding temperature beyond 650°C. MK-D61 hardware usually contained 61 fuel pins (see Figure 2-6). However, as EBR-II enforced a subassembly mean coolant outlet temperature of 544 °C, 12 solid dummy fuel pins were included to reduce the subassembly total power. Then 19 HT9 clad and 30 D9 clad U-10Zr fuel pins were irradiated in the subassembly X447 to a burnup around 4.7 at.%. Then four HT9 pins were replaced with fresh fuel pins before the irradiation experiment continued as subassembly X447A until an ultimate burnup of approximately 10 at.%. In the X447/A experiment, all the HT9 pins were located in the center region of the subassemblies to develop high cladding temperature, while the D9 pins were located in the peripheral region along with dummy pins. In the presence of adjacent dummy pins, all the D9 clad pins experienced much lower irradiation temperatures and thus had no issues surviving ~10 at.% burnup. At the end, among the 15 HT9 clad fuel pins irradiated to approximately 10 at.%, the cladding of two pins (DP70 and DP75) were found to have breached during the steady-state high-temperature irradiation. The cladding failure occurred near the top of the fuel slugs, corresponding to the peak cladding temperature locations. More importantly, severe FCCI wastage formation and prominent CCCI

wastage formation were observed in those HT9 clad pins irradiated to ~ 10 at.%. In some cases, over one-third of the cladding thickness was consumed by wastage formation (see Figure 2-1 for an example). Thus, the HT9 cladding failure observed in X447/A was determined to originate from a combined effect of wastage-induced cladding degradation and thermally-activated creep rupture. X447/A was a valuable experiment for FCCI/CCCI study because the wastage formation effects were prominent. In general, this experiment was important for HT9 cladding as it defined the operating condition envelope of applying HT9 cladding in SFRs. Therefore, only the HT9 clad pins in X447/A experiment were investigated in this evaluation effort. In particular, four pins with most PIE data available (i.e., DP04, DP11, DP70, and DP75) are the focus in this report.

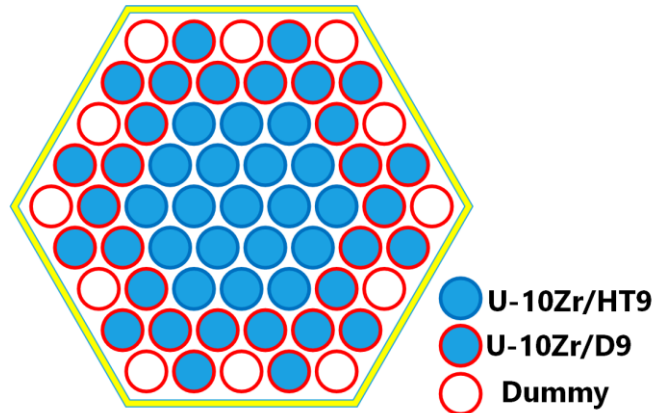


Figure 2-6 Schematic showing the U-10Zr/HT9 pins locations in X447/A subassembly.

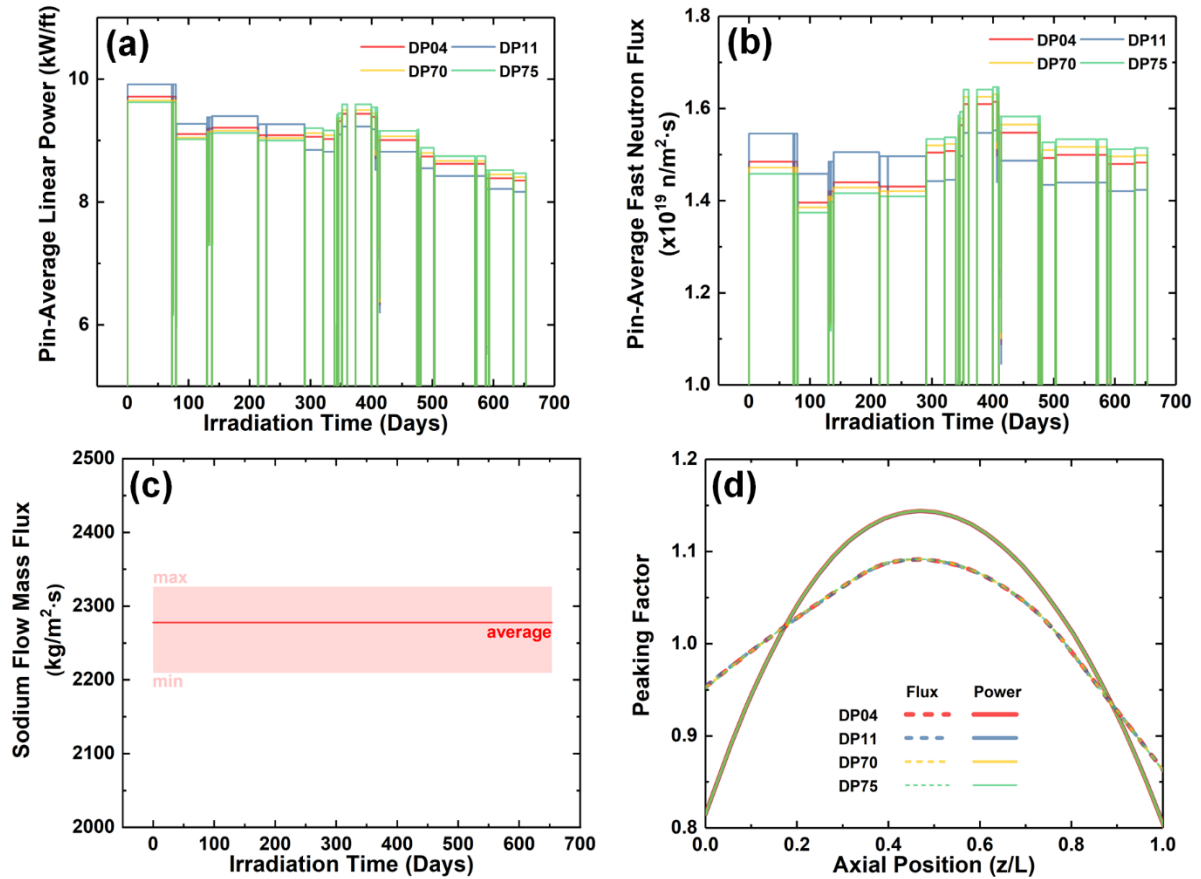


Figure 2-7 Typical FIPD-based input data used for BISON simulation focused on FCCI/CCCI.

First, all the pin design geometry parameters were directly adopted from the pin design/fabrication available at FIPD. The CSV format file for the data was directly read by BISON's built-in automatic Mesh Generator object, developed under the BISON-FIPD integration project. The time-dependent pin-by-pin irradiation condition parameters, such as power history and peaking profile, fast neutron flux history and peaking profile, and coolant mass flow flux history, were directly adopted from BISON Input Functions CSV files, downloadable from FIPD, that can be directly read by BISON. The key irradiation condition parameters of the four representative HT9 clad pins irradiated in X447/A are illustrated in Figure 2-7. It is clear that the pin-average fast flux was relatively stable and ranged approximately from 1.4 to 1.6×10^{19} n/m².s (Figure 2-7(b)). Meanwhile, due to the depletion of the fuel, the pin-average linear power decreased from an initial ~ 10 kW/ft to ~ 8 kW/ft near the end of irradiation (Figure 2-7(a)). The sodium coolant mass flow flux of the X447/A experiment was relatively stable, ranging from ~ 2200 to ~ 2350 kg/m².s (see Figure 2-7(c)). On the other hand, within X447 and X447A subassemblies, pin-by-pin difference in axial fast flux and power profiles was marginal, as shown in Figure 2-7(d).

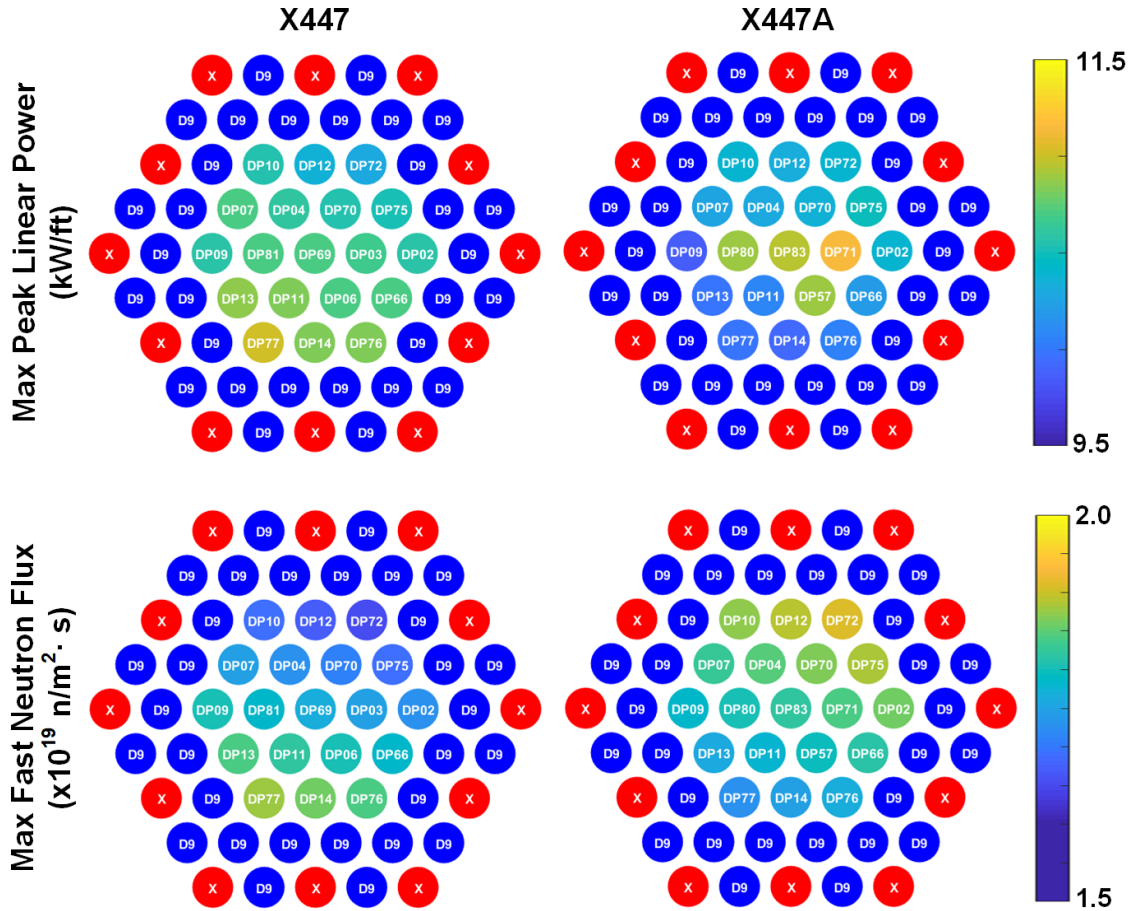


Figure 2-8 Pin-by-pin maximum peak linear power and fast neutron flux of the U-10Zr/HT9 pins in X447/A Subassembly.

A more comprehensive comparison of FIPD-based irradiation conditions is indicated in Figure 2-8. In X447, the lower left corner of the subassembly shown in Figure 2-8 experienced a higher fast neutron flux compared to the upper right corner, because it is farther away from a control rod. During the X447 to X447A reconstitution, the subassembly was rotated by 180° . As a result, the fast neutron flux profile flipped. In X447, as all the fuel pins were fresh, the power profile exactly follows the fast flux profile. On the other hand, the four fresh pins (i.e., DP57, DP71, DP80, and DP83) inserted during X447 to X447A reconstitution experienced prominently higher power compared to their neighboring pins already irradiated in X447.

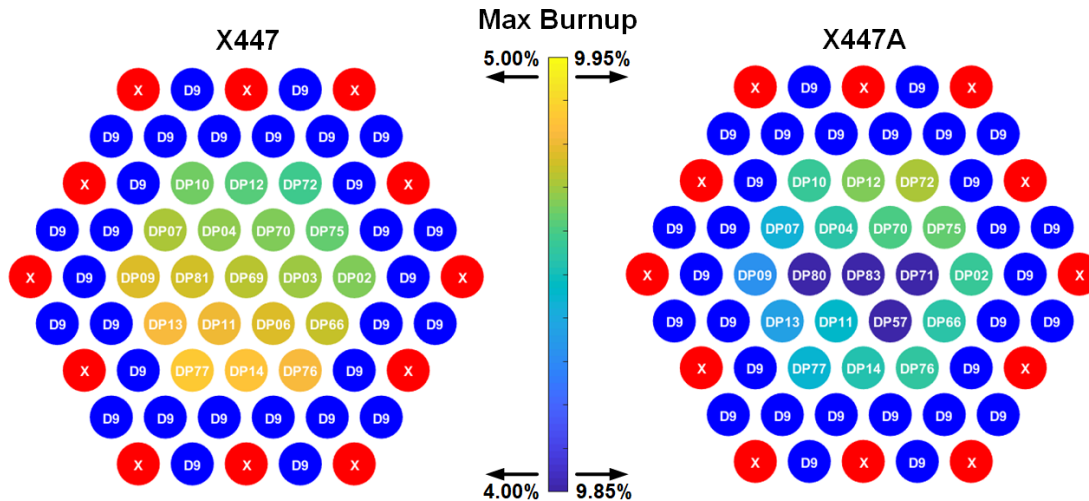


Figure 2-9 Pin-by-pin maximum burnup of the U-10Zr/HT9 pins in X447/A Subassembly.

After the X447/A irradiation experiment, 15 HT9 clad fuel pins irradiated in both subassemblies had approximately 9.9 at.% peak burnup, while the other eight HT9 clad fuel pins that were irradiated in either of the subassemblies had approximately 5 at.% burnup, as shown in Figure 2-9.

2.4.2 Evaluation Results and Discussion

Before discussing the FCCI/CCCI phenomena and their consequences, as predicted by the BISON models implemented in this study, it is worth examining some crucial condition parameters predicted by other BISON models. Because these condition parameters are closely related to the formation kinetics of FCCI/CCCI wastage and cladding damage and deformation, looking into them will help understand the BISON predicted FCCI/CCCI, kinetics and cladding degradation that will be focused on later.

2.4.2.1 *BISON Calculated Condition Parameters*

One of the most important calculated condition parameters is temperature. As a statistical measure of thermal energy, temperature is the driving force for many fuel performance phenomena, including FCCI, CCCI and cladding deformation. The time evolution of the peak cladding temperature calculated by BISON using two available coolant channel models based on FIPD power and coolant flow rate history is listed in Figure 2-11. Also listed is the corresponding information recorded in FIPD based on SuperEnergy2 [25] simulation (the effective maximum power time or EMPT version). The temperatures predicted by SuperEnergy2 were compared with measured EBR-II temperature and indicated reasonably good agreement [26]. By comparing the four representative fuel pins shown in Figure 2-11, it is prominent that both BISON coolant channel models predict slightly higher peak cladding temperatures compared to temperature given in FIPD.

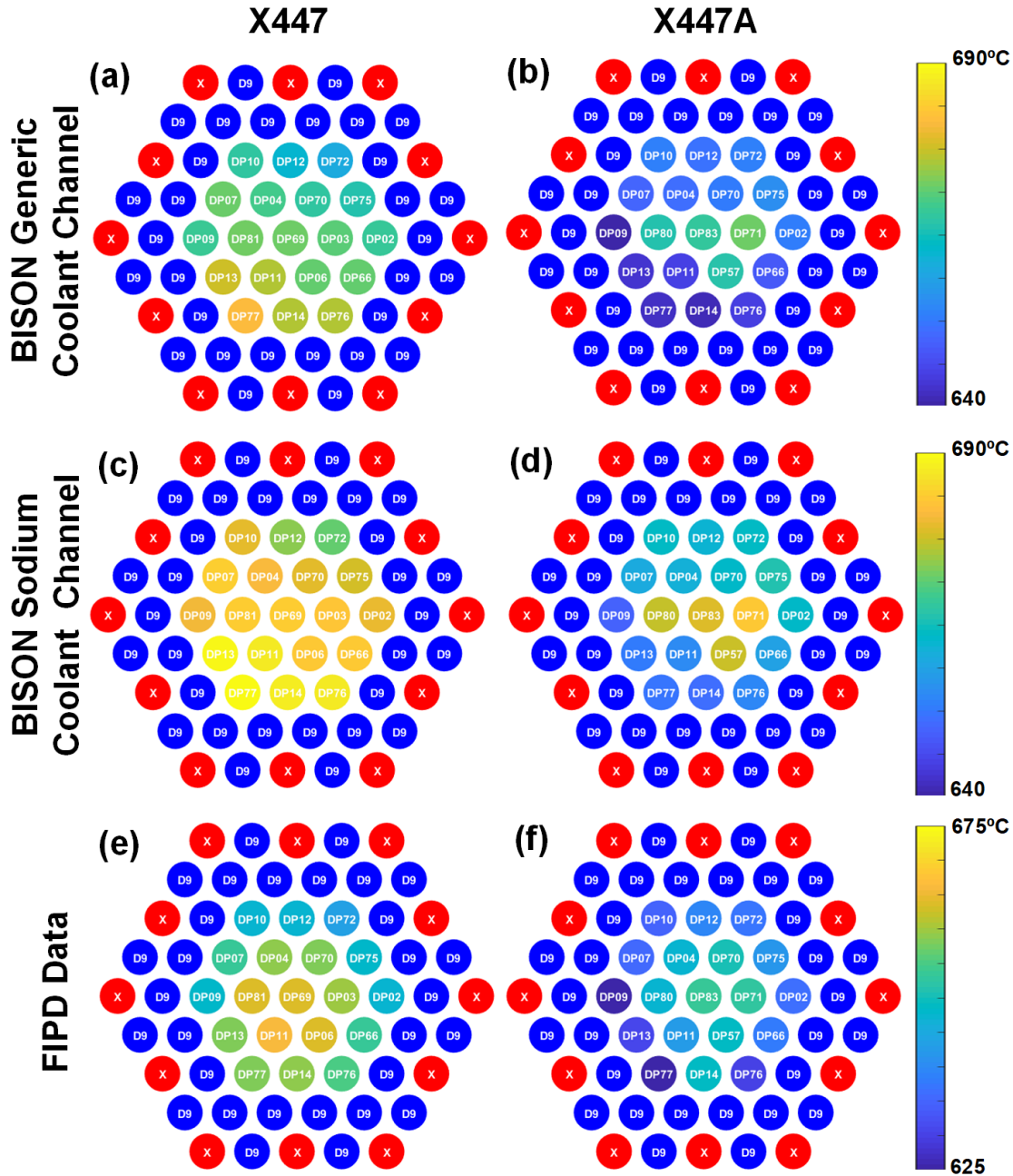


Figure 2-10 Comparison between BISON-predicted peak cladding temperatures and FIPD-recorded peak cladding temperatures indicating the limitations of current BISON coolant channel model.

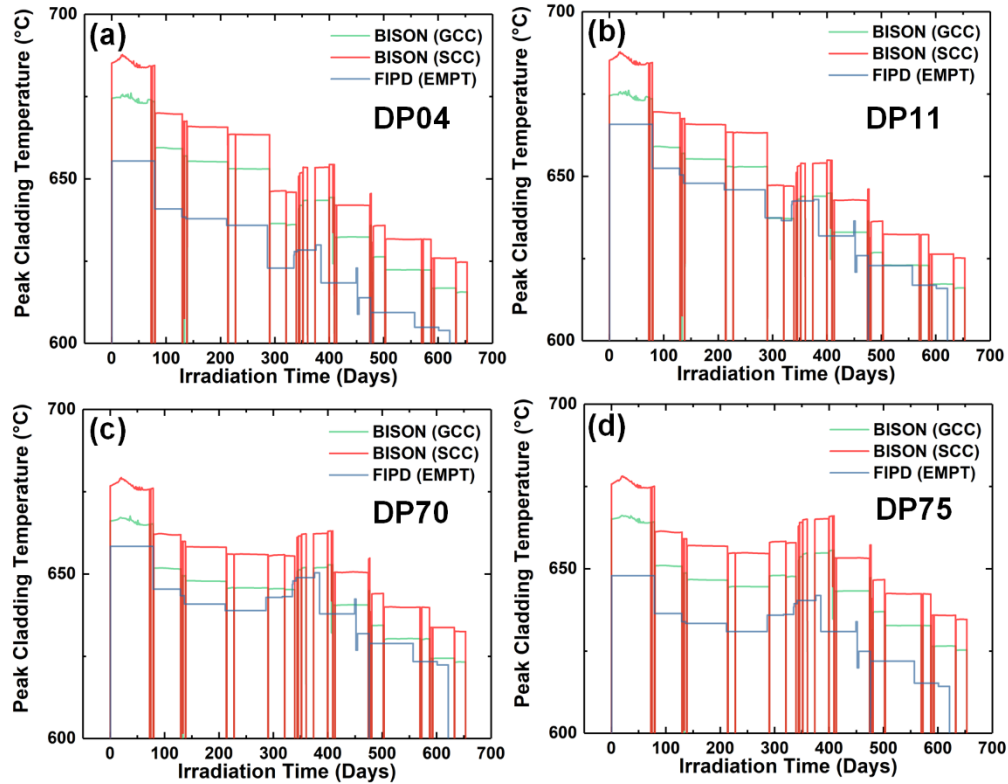


Figure 2-11 Time-evolution of peak cladding temperature for four representative pins.

A more comprehensive comparison can be found in Figure 2-10. As the SuperEnergy2 calculation considers the influence from those twelve zero-power dummy fuel pins, the predicted cladding temperature is relatively lower, especially for those pins near the peripheral region of the subassembly. On the other hand, as BISON’s coolant channel models assume an infinite lattice of the exact same kind of pin, these models effectively neglect the contribution from other pins in the subassembly, especially when the other pins have different power. As a result, the influence of those dummy pins on temperature was not taken into account, leading to an approximately 5~25 °C temperature difference in comparison to FIPD data. This may lead to slight overestimate of all thermally driven phenomena simulated by BISON. It is also noticeable that BISON’s generic coolant channel model predicts peak cladding temperature slightly lower than that predicted by BISON’s dedicated sodium coolant channel model. For some runs, the peak cladding temperatures predicted by the generic coolant channel model are even comparable to values stored in FIPD. Thus, both models were used in this study to provide ideas about the sensitivity of related models to temperature.

Additionally, the fuel cladding deformation is mainly caused by different phenomena including, cladding irradiation-induced swelling, thermal and irradiation creep induced by fuel-cladding mechanical interaction (FCMI) and plenum pressure. Irradiation swelling in HT9 is marginal and is usually neglected in fuel performance analysis [27]. Considering the ~10 at.% peak burnup and 75% smeared density for X447/A HT9 clad fuel pins, the FCMI effect is marginal as the fuel-cladding contact is still “soft” due to the hot-pressing effect [28], [29]. Therefore, cladding deformation induced by the high temperature and plenum pressure induced stress was the major

source of the cladding deformation in this experiment. This is consistent with the observation that the maximum cladding deformation and failure were always observed near the top of the fuel position in this experiment. During irradiation, the plenum pressure continued to increase due the fission gas release. Thus, reliable and consistent fission gas release prediction is important for high-fidelity simulation of cladding in X447/A. In Figure 2-12(a), BISON predicts that fission gas release starts after ~50 days of irradiation and ultimately approaches ~71% fractional fission gas release. This value is close to the measured value of 72%~76% in the X447/A PIE results. This ~71% fission gas release leads to a plenum pressure of 9 MPa near the end of the irradiation, as shown in Figure 2-12(b).

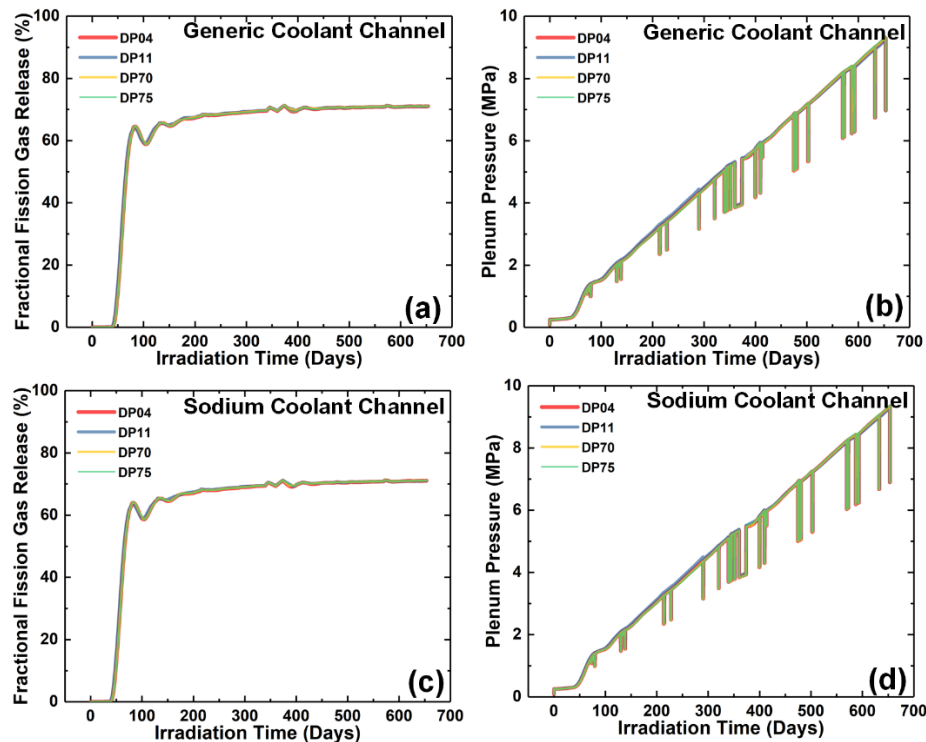


Figure 2-12 Fission gas release (FGR) data predicted by the BISON code for the four representative pins irradiated in X447/A subassembly: (a) time evolution of fractional fission gas release using BISON's generic coolant channel; (b) time evolution of plenum pressure using BISON's generic coolant channel; (c) time evolution of fractional fission gas release using BISON's sodium coolant channel; (d) time evolution of plenum pressure using BISON's sodium coolant channel. Note that the FGR behaviors predicted by the two coolant channel models are similar because the FGR is less sensitive to temperature compared to other behaviors such as FCCI/CCCI.

2.4.2.2 BISON Predicted FCCI/CCCI Wastage

Based on the calculated irradiation conditions discussed in the previous subsection, the evolution of both FCCI and CCCI wastage layer thickness was predicted by BISON for all 15 HT9 clad fuel pins irradiated in X447 and X447A subassemblies to ~10% burnup. The calculated FCCI and CCCI wastage thickness at the end of the irradiation is illustrated in Figure 2-13. The data of the four

representative fuel pins are plotted as lines, while the ranges of the FCCI/CCCI data are expressed as orange and blue areas.

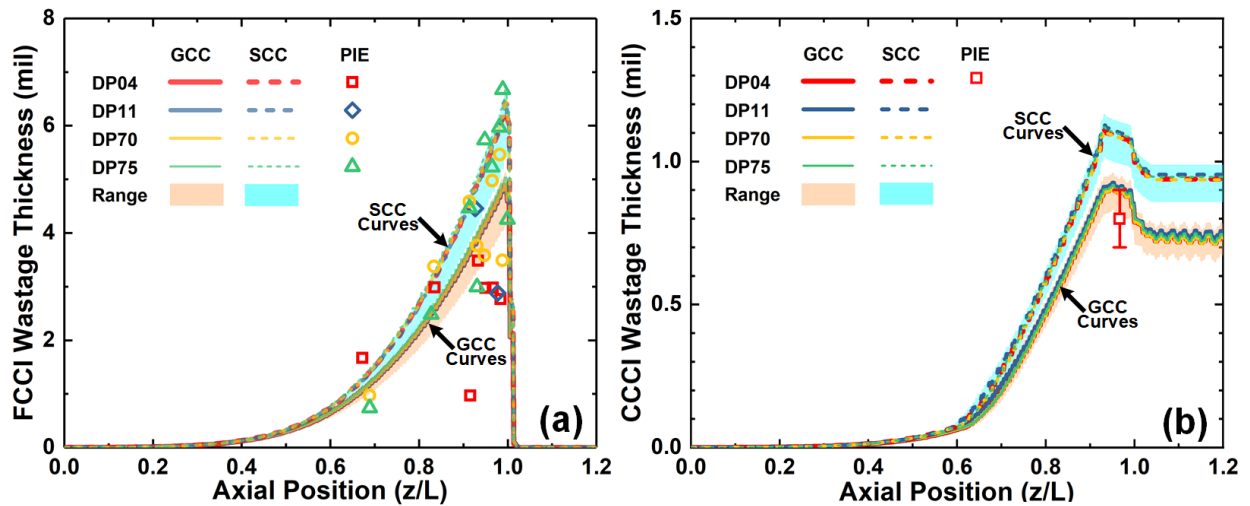


Figure 2-13 FCCI and CCCI wastage thickness of 15 HT9 clad pins irradiated in both X447 and X447A subassemblies: (a) FCCI wastage predicted by BISON using both BISON’s generic and sodium coolant channel (GCC/SCC) models compared to PIE data [19]; (b) CCCI wastage predicted by BISON using both BISON’s generic and sodium coolant channel (GCC/SCC) models with measured CCCI wastage thickness from DP04. Note that the measured CCCI thickness only contains carbon depletion layer (d_{cd}) and is thus lower than both BISON predicted values.

Due to the different predicted cladding temperature by the two coolant channel models, the slightly higher cladding temperature predicted by the dedicated sodium coolant channel model led to a slightly higher FCCI/CCCI wastage thickness. As shown in Figure 2-13(a), the maximum predicted FCCI wastage using the sodium coolant channel model is approximately 1 mil or 25 microns thicker than that predicted by the generic coolant model. The predicted FCCI wastage thickness values are consistent with the PIE data of the four representative HT9 clad pins. The difference in calculated FCCI wastage and temperature may still cause discrepancies in cladding degradation and deformation, which will be discussed later in this paper. In addition, as mentioned early in this paper, due to the limit of BISON’s current coolant channel models, the cladding temperatures of some HT9 clad fuel pins were overestimated. Thus, using the two different coolant channel models that predict slightly different cladding temperatures may provide an alternative way to help understand the different behaviors of central and peripheral HT9 clad fuel pins. On the other hand, as shown in Figure 2-13(b), the predicted CCCI wastage thickness values using the two coolant channel models have a minor difference of approximately 0.2 mil or 5 microns, which could be neglected compared to the influence of the difference in predicted FCCI wastage thickness values.

2.4.2.3 Cladding Degradation and Deformation

With the irradiation condition (mainly temperature and plenum pressure) and FCCI/CCCI wastage formation predicted by the corresponding BISON correlations, the deformation and damage of the HT9 cladding were then calculated by BISON’s tensor mechanics modules with and without

implementation of the cladding degradation model. One of the major measures that is used to quantify the damage of HT9 cladding in SFRs is the cumulative damage fraction (CDF). The steady-state CDF model available in BISON was used in this study [20], [30]. The maximum CDF values at the end of irradiation found in all the HT9 clad fuel pins irradiated in X447 and X447A subassemblies are illustrated in Figure 2-14.

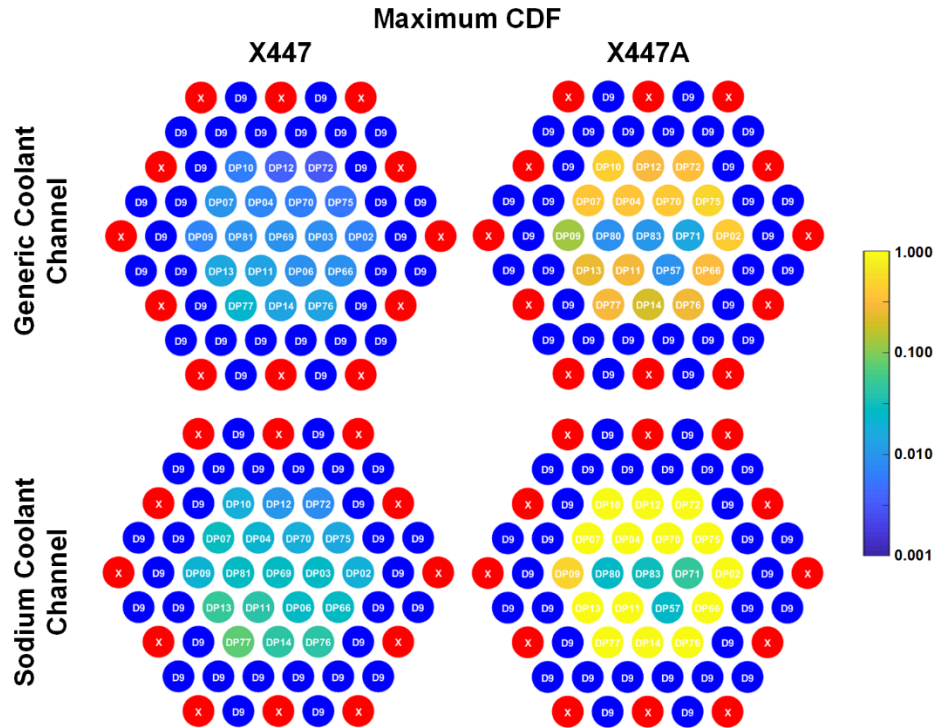


Figure 2-14 Maximum CDF of all HT9 clad fuel pins irradiated in X447 and X447A subassemblies predicted by BISON using both generic and sodium coolant channel models.

Due to the different peak temperatures predicted by the two coolant channel models available in BISON, using the sodium coolant channel generally yields higher CDF values compared to the other option. After ~5% burnup, both coolant channel models lead to CDF values lower than 0.05, which is the safety criterion defined in IFR Mark V safety report [31]. However, after ~10% burnup, BISON predicts approximately 0.35 and 1.00 CDF values using generic and sodium coolant channel models, respectively, exceeding IFR Mark V fuel safety criterion. These predicted CDF values suggest a significant failure possibility under the irradiation conditions involved in the X447/A experiment after ~10 at.% burnup. This is consistent with the experimental observation of two failed pins out of the 15 HT9 clad fuel pins irradiated to ~10% burnup in X447/A. It is also worth mentioning that without the introduction of the cladding degradation model, the maximum CDFs of those HT9 clad fuel pins irradiated to ~10% burnup are around 0.1 and 0.2 using generic and sodium coolant channel models, respectively, which are much lower compared to the two out of fifteen failures observed.

More insights can be obtained by looking into the CDF analysis. Based on the IFR Mark V safety analysis criterion, the HT9 cladding CDF can be quantitatively related to failure probability. More

specifically, the cladding failure probability follows normal distribution of the logarithm of the CDF value with a mean logarithmic CDF (μ) of -0.0354 and a standard deviation (σ) of 0.1885. The cumulative probability distribution can then be plotted as shown in Figure 2-15(a).

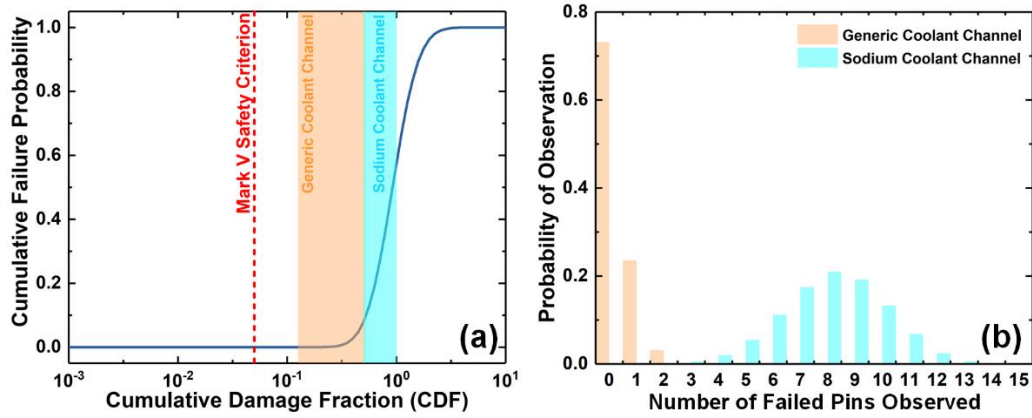


Figure 2-15 Comparison between BISON predicted CDF and observed failed pins during X447/A experiment: (a) BISON predicted CDF ranges and corresponding failure probability based on the correlation described in Ref. [31]; (b) Probabilities of observing a specified number of failed pins predicted by BISON using the two coolant channel models.

Therefore, the 0.05 maximum CDF as regulated in the Mark V safety analysis corresponds to a failure probability of approximately one in one hundred billion. Also shown in Figure 15(a) are the maximum CDF ranges of the HT9 cladding pins predicted by BISON using both coolant channel models. Based on the two sets of CDF value predicted for the 15 HT9 clad pins, the probabilities of observing different numbers of failed pins can be deduced. For each of the 15 (N) pins of interest in this study, the failure probability determined by CDF is $p_{f,i}$ with $i = 1, 2, \dots, N$. For a given observed failed pin number N_f , there are $\binom{15}{N_f}$ different possible combinations. For a specific combination, the failed pin indices are $i_f = 1, 2, \dots, N_f$; and survived pin indices are $i_s = 1, 2, \dots, (15 - N_f)$. The probability of observing such a combination is $\prod_{i_f=1}^{N_f} p_{f,i_f} \prod_{i_s=1}^{15-N_f} (1 - p_{f,i_s})$. Then, the probability of observing N_f failed pins can be deduced by summing up all the $\binom{15}{N_f}$ terms of $\prod_{i_f=1}^{N_f} p_{f,i_f} \prod_{i_s=1}^{15-N_f} (1 - p_{f,i_s})$. The results are summarized in Figure 2-15(b). The CDF values based on BISON's generic coolant channel model correlate to zero or one failed pins, whereas the sodium coolant channel leads to a maximum likelihood failure pin number of eight. Compared to the two failure pins actually observed in X447/A experiment, the CDF values are expected to be in between the results based on the two BISON coolant channel models. This finding is consistent with the previous discussion: (1) two coolant channel models predict temperatures that differ by $\sim 10^\circ\text{C}$; and (2) those HT9 clad pins near the peripheral region experienced a lower cladding temperature. That is, the actual cladding damage behavior approximately between the BISON predictions using the two different coolant channel models.

Another important cladding behavior is its plastic deformation. Unlike the CDF, which is a statistical concept that cannot be directly measured, cladding deformation after in-pile irradiation can be experimentally obtained by measuring cladding outer diameter [19]. In the X447/A experiment, both contact profilometry and laser profilometry were used to measure the cladding outer diameter after irradiation. These profilometry data can be compared with the cladding outer diameters predicted by BISON for evaluation. Note that HT9 CCCI wastage layer calculated by BISON contains both corrosion mass loss and carbon depletion layer. The corrosion mass loss component needs to be removed from the BISON predicted cladding outer diameter before comparing with the PIE data. The cladding outer diameter profiles of the four representative HT9 clad fuel pins are illustrated in Figure 2-16. Those cladding diameter changes are mainly a result of thermal creep of the HT9 cladding facilitated by cladding degradation due to FCCI/CCCI.

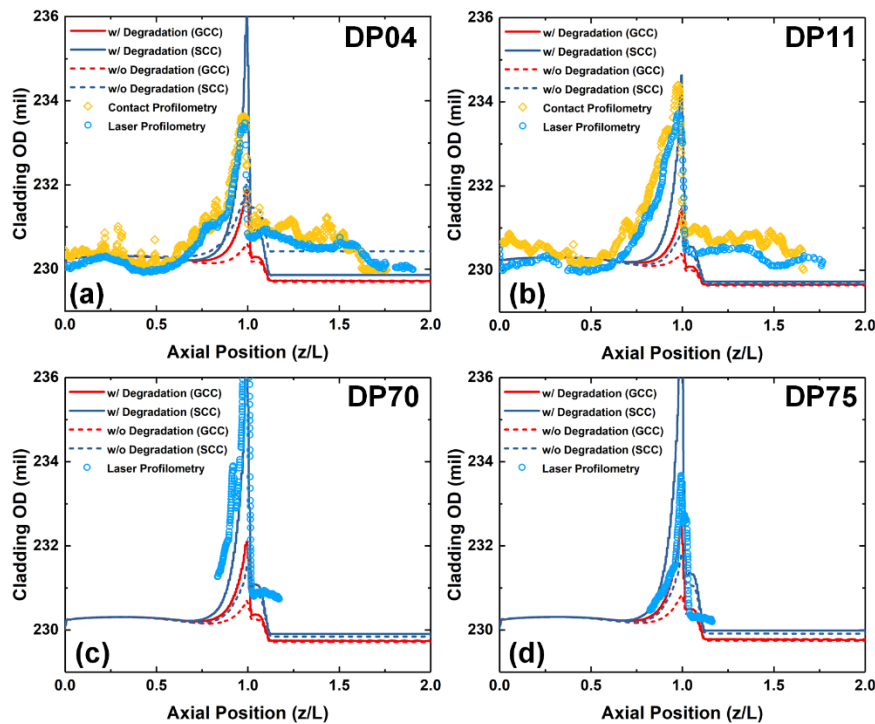


Figure 2-16 BISON predicted cladding deformation of four representative HT9 clad fuel pins irradiated in X447/A subassembly compared with PIE data [19], [32].

It is clear that the introduction of the cladding degradation model in this study significantly increased the cladding deformation, indicating the importance of having a credible cladding degradation model for reliable cladding deformation simulation. For fuel pin DP11 (see Figure 2-16(b)), BISON is capable of predicting cladding outer diameter (OD) profiles that are comparable with profilometry data when using the sodium coolant channel model. Meanwhile, BISON with the generic coolant channel model, underestimates the cladding outer diameter after irradiation of this pin. For fuel pins DP04 and DP70 (see Figure 2-16(a) and (c)), the measured cladding diameter profiles fall between the BISON predicted values using the two different coolant channel models. Meanwhile, for fuel pin DP75 (see Figure 2-16(d)), the PIE cladding outer diameter is more consistent with the BISON prediction using the sodium coolant channel model. Therefore, using

the current BISON-FIPD simulation setup, neither the generic nor the sodium coolant channel models can provide cladding deformation profiles that are globally accepted for all fifteen fuel pins.

Again, the issue originates from the limitation of the current BISON coolant channel models, which neglect the contributions from adjacent fuel pins. For those fuel pins located near the dummy pins, such as DP75, BISON with the generic coolant channel models produces a cladding deformation similar to profilometry measurements, because the lower predicted temperature better emulates the temperature reduction effect of the dummy pins. For those fuel pins located near the center of the subassembly (away from the dummy pins), BISON with sodium coolant channel models performs well in predicting cladding deformation compared to PIE results because of the higher predicted cladding temperatures. More importantly, in X447/A subassembly, the four fresh fuel pins (i.e., DP57, DP71, DP80, and DP83, which were added to the experiment as part of the experiment reconstitution into the subassembly after the original pins were taken out from X447 for destructive or non-destructive PIE) had a higher power, affecting the local temperature profile. For example, fuel pin DP04, DP11, and DP70 were all located near the center of the subassembly. However, three of the six adjacent pins of DP11 were fresh pins while only two of the six pins adjacent to DP04/DP70 were fresh pins (see Figure 2-6). As a result, the actual cladding deformation of DP11 is closer to the BISON prediction using sodium coolant channel models, while the profilometry measurement data of pins DP04 and DP07 are between the BISON data using the two different coolant channel models. This again emphasizes the importance of developing an improved cladding temperature boundary condition approach that takes adjacent pins into consideration.

Therefore, it is clear that the implementation of a cladding degradation model based on a degradation factor dependent on FCCI/CCCI wastage thickness enables the cladding deformation simulation in BISON considering FCCI/CCCI effects. This implementation also improves BISON's capability of predicting CDF and cladding deformation that are consistent with PIE observations. However, using the current BISON-FIPD integration framework, the performance of the cladding damage and deformation simulation is limited by the selection of coolant channel models. As shown in Figure 2-17, statistically, BISON with sodium coolant channel models predicts cladding deformation more consistent with PIE profilometry data of those X447/A fuel pins experiencing higher irradiation temperature (i.e., located near the center of the subassembly), while BISON with generic coolant channel models performs better for those X447/A fuel pins near the dummy pins. Hence using both coolant channel models may work as a temporary approach for X447/A subassembly simulations. However, a different approach is still needed for improving the performance of BISON simulation within BISON-FIPD integration framework.

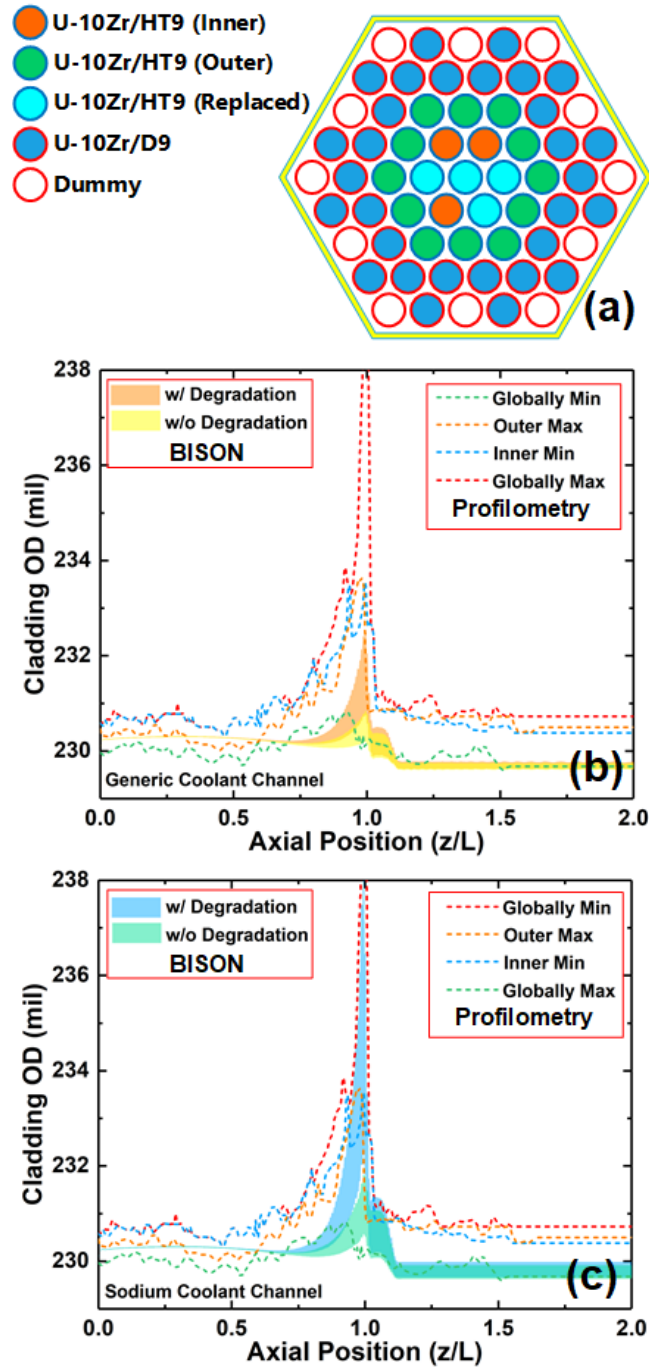


Figure 2-17 Statistical fuel cladding outer diameters of all 15 HT9 clad fuel pins irradiated in both X447 and X447A subassemblies: (a) a diagram showing the three different categories of HT9 clad pins: inner (located near the subassembly center), outer (located near the dummy pins), and replaced (replaced with fresh pins during reconstitution); (b) range of predicted cladding deformation using generic coolant channel model; (c) range of predicted cladding deformation using sodium coolant channel.

2.4.2.4 Guidance for Future Improvements

As mentioned in the previous subsections, the major limitations on BISON simulation performance are the existing coolant channel models, both of which were developed on simplified thermal hydraulic correlations based on a single pin's power with periodical boundary condition. In this regard, an improved temperature boundary condition approach that takes the adjacent fuel pins into account is required. Such new approach will not affect those subassemblies containing fuel pins with similar linear power, whereas it will be effective for those subassemblies involving fuel pins with different linear power due to dummy pins, reconstitution, or different fuel compositions, etc.

Under the current FIPD-BISON integration framework, the most straightforward approach is to directly apply the coolant temperature or cladding outer surface temperature available in FIPD to be boundary conditions. Those temperature data were calculated by SuperEnergy2, which is a dedicated thermal hydraulic code that simulates multiple subassemblies simultaneously and takes into account cross flow within a subassembly. Therefore, these temperature data not only consider the contribution of neighboring fuel pins, but also adjacent subassemblies (that could be a control subassembly or other lower power subassemblies).

In the current FIPD data, only constant sets of temperatures are provided for different EBR-II runs. That is, there is no temperature variation within in each EBR-II run. In order to be compatible with the other FIPD-based BISON input data, which are all time-dependent, pin-by-pin time-dependent coolant/cladding temperature data needed developed and made available to all FIPD users. This effort is a focus of FIPD-BISON integration efforts. Once the time-dependent temperature boundary condition data are ready, the FCCI model parameters will also be re-calibrated based on the PIE measurement and new models. By making these improvements, it is expected that BISON can produce CDF and cladding deformation profiles for all fuel pins using a uniform setup. The detail of the aforementioned effort is discussed in the next Chapter.

3 FIPD-Informed Temperature Boundary Conditions

As discussed in Chapter 2, cladding temperature calculation using BISON's intrinsic coolant channel models have a series of limitations, especially in the cases when adjacent fuel pins have dissimilar powers. Therefore, it would be beneficial to enable an option in BISON so that the users can easily use the pin-by-pin cladding outer surface temperature profiles available in FIPD, which are calculated by the thermohydraulic code SuperEnergy2. In this Chapter, the development of time-varying cladding temperature profiles in FIPD is first introduced. Then the corresponding BISON object that reads and uses such data for temperature boundary condition is described. Finally, the advantages of directly using FIPD-based temperature boundary conditions are discussed using the X447/A experiment as an example.

3.1 Development of Time-Varying Temperature in FIPD

Fuel performance simulation involves complex kinetics that are sensitive to irradiation conditions, especially temperature. Accurate prediction of temperature profile is the foundation of high-fidelity fuel performance simulation. In BISON, temperature calculation is performed by solving the thermal diffusion equation of the entire fuel-cladding system. Therefore, accurate temperature boundary conditions defined on the cladding outer surface is key to obtaining high-quality temperature predictions. In this section, the procedure of a pin-by-pin cladding outer surface calculation is described along with the data structure available to FIPD users who are interested in a BISON simulation under an BISON-FIPD integration scope.

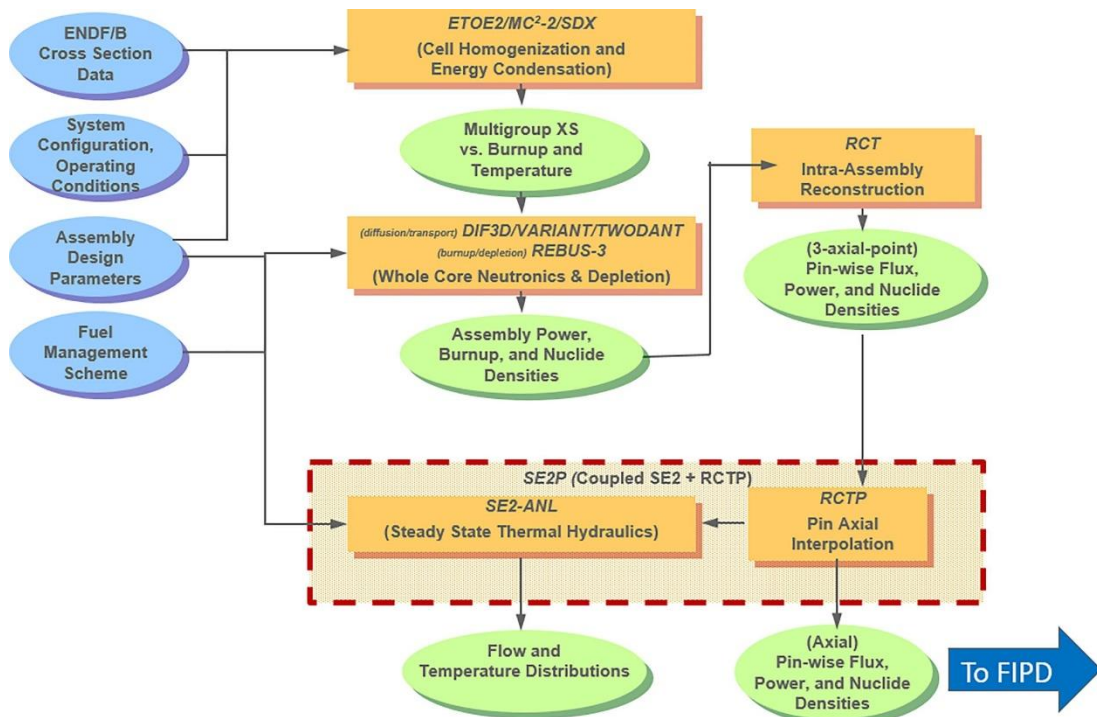


Figure 3-1 Overview of the computer codes and data used to calculate the operating parameters presented in FIPD[33].

In FIPD database, a series of legacy codes are used to calculate pin-by-pin operating parameters, as shown in Figure 3-1. In the original FIPD, for each EBR-II run, only an average power over the irradiation period was available. This average power is calculated by dividing the deposited energy throughout that EBR-II run by the run duration approximated by the calendar day difference between the start and end dates of the run. Therefore, this average power may include considerable error when the run duration is short or when the power fluctuation is significant. Therefore, in FY2020, time-varying power of EBR-II was recovered from EBR-II run reports as well as EBR-II digital data acquisition system (DAS) records. This power history data was used to scale pin-by-pin power of each EBR-II run to produce pin-by-pin power history data (see Figure 2-7(a) for examples). Using the same approach illustrated in Figure 3-1, the time-varying pin-by-pin coolant temperature and cladding outer surface temperature profiles are calculated for all the pins. In Figure 3-2, the calculated time-varying peak cladding outer surface (found near the axial position corresponding to the fuel top) is illustrated. On the other hand, the axial profile of the cladding outer surface temperature can be found in Figure 3-3, which is the maximum value of each axial position throughout the irradiation time. As shown in Figure 3-3, the axial position is provided in the form of fractional coordinates (z/L , z is the distance from fuel bottom and L is the fuel axial length) to provide more flexibility in the presence of fuel axial growth due to swelling.

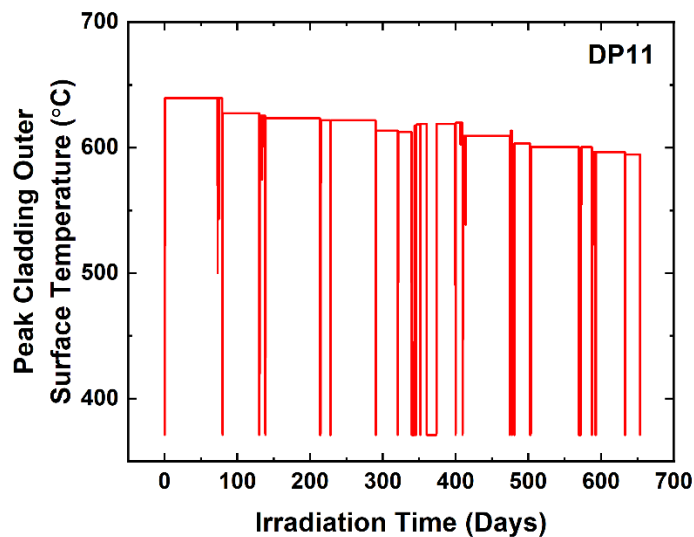


Figure 3-2 Time-dependent peak cladding temperature in FIPD.

These data are provided on FIPD website as part of the “BISON Input Function” data page of each pin. The data are provided in both plain text web data as well as CSV files. The CSV files are downloadable and can be directly used by BISON using the object described in the next Section.

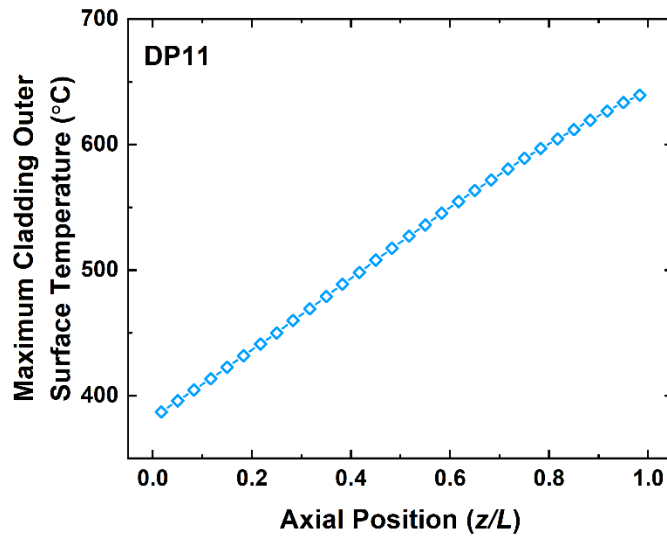


Figure 3-3 Maximum cladding temperature at different axial positions.

3.2 Utilization of the Time-Varying Temperature in BISON

In order to facilitate the use of the FIPD for BISON simulation, a BISON Functions object `FIPDAxialProfileFunction` was developed. This object generates a Function based on the axial profile CSV files available at the FIPD. Currently, it can be used to import two types of FIPD data:

- (1) time-dependent axial peaking factor profiles of linear power and neutron flux;
- (2) time-dependent axial temperature profiles of coolant and fuel components to be used as boundary conditions (BCs) for thermal analyses.

The CSV data files to be imported by the `FIPDAxialProfileFunction` object have a similar format as the data files used by the `PiecewiseBilinear` object. The major difference is that the fractional axial position (z/L or y/L) instead of absolute position is used as the axial abscissa. This approach is selected so that users can use their own arbitrary pin geometry parameters. More importantly, mesh metadata from `FIPDRodletMeshGenerator` can be directly adopted to convert the fractional axial positions to absolute position values to ensure consistent use of geometry parameter throughout the simulation.

As fractional axial coordinates are obtained from the FIPD-based CSV data file, `FIPDAxialProfileFunction` needs to convert the fractional coordinates into absolute axial coordinates. To do this, three pin geometry parameters are needed: `bottom_clad_height` (d_{bottom} , thickness of cladding bottom end plug), `clad_bottom_gap_height` (d_{gap} , gap distance between the end plug and the bottom of the fuel slug), and `fuel_slug_length` (L_{fuel} , the axial length of the fuel slug). The absolute axial coordinates (y) then have the following expression (Equation (3-1)):

$$y = (d_{bottom} + d_{gap}) + \frac{y}{z} L_{fuel} \quad (3-1)$$

The three pin geometry values can either be directly input by users in the input block of this object or taken from FIPDRodletMeshGenerator mesh generator as mesh metadata variables (i.e., cladding_start, cladding_bottom_gap_width, and fuel_height).

During fuel depletion, the axial length of the fuel is subject to change due to fuel swelling and thermal expansion. In order to take this effect into consideration, a postprocessor can be set up to track the displacement of the fuel slug top. The postprocessor value can then be imported into this object as fuel_elongation_pp so that the fuel slug axial length L_{fuel} can be updated during the time iteration.

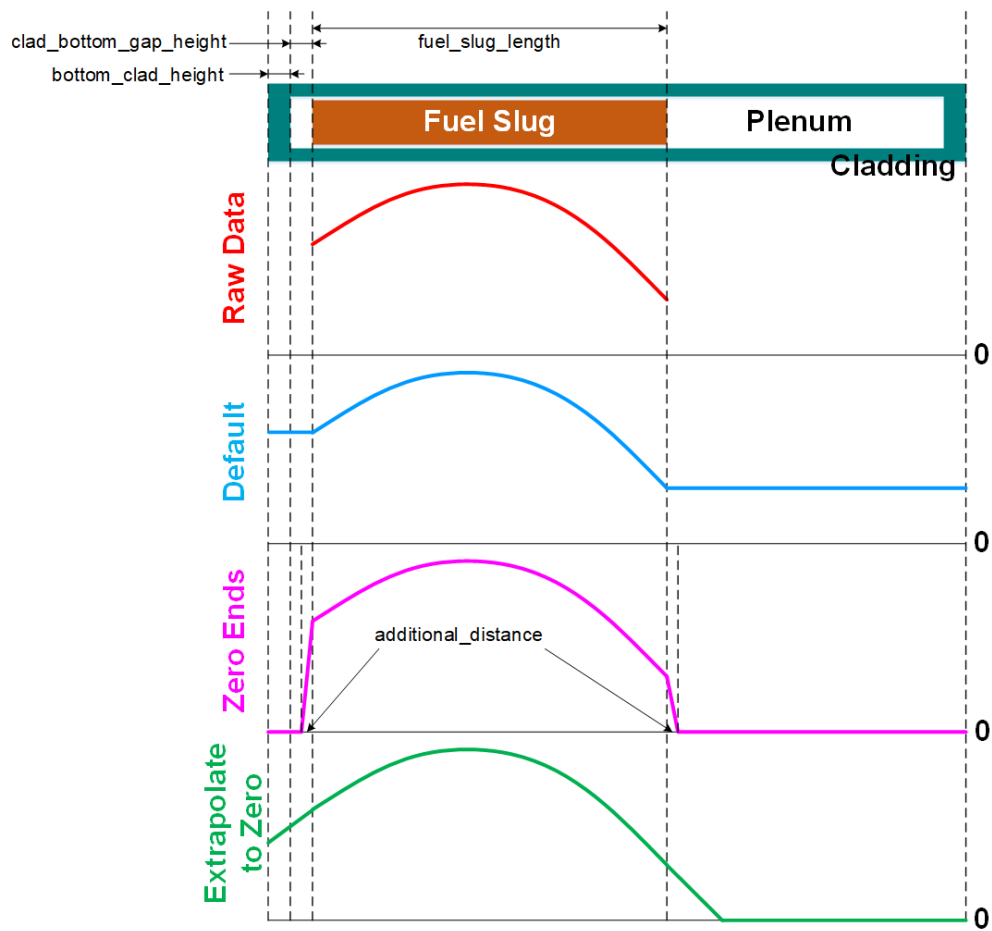


Figure 3-4 a schematic drawing showing different options in FIPDaxialProfileFunction to process values beyond fuel end positions.

Additionally, this object adopts MOOSE's BilinearInterpolation class for Functions generation. By default, beyond top or bottom position of the fuel, a constant value that is equal to the value at either of the fuel ends is taken as the function value. If zero_end is set as true, the FIPDaxialProfileFunction object reduces the function value linearly to zero over a distance

that is defined by an optional input `additional_distance`. Another useful alternative functionality is to extrapolate the function values to zero beyond the two ends of fuel. This functionality is specifically useful to extrapolate fuel fast neutron flux for cladding models such as swelling and creep. This functionality can be activated by setting `extrapolate_to_zero` and `zero_end` as `true`. More details about these options can be found in Figure 3-4.

After the axial profile function is imported from the CSV data file and is processed on both fuel ends, further processing can be achieved by setting shifting (s) and scaling (f) values (see Equation (3-2)). A common use of this processing is to converting units (e.g., Celsius to kelvin).

$$v = f(v_0 + s) \quad (3-2)$$

To use this `FIPDAxialProfileFunction` object to enable FIPD-based temperature boundary conditions, the time-varying cladding outer surface temperature profile CSV file needs to be converted into a MOOSE Function by `FIPDAxialProfileFunction`. Then the `FunctionDirichletBC` is used to assign this MOOSE function as the Dirichlet boundary condition for temperature on the cladding out boundary. This approach is used throughout the report.

3.3 Advantages of the New Approach

The BISON assessment based on X447/A experiment that is described in Section 2.4 is re-investigated in this Section by utilizing the newly implemented FIPD-based temperature boundary conditions so as to evaluate the advantages of the new approach.

While the majority of the simulation parameters should be the same for the re-investigation, the empirical FCCI correlation parameters need to be updated. In FY2020, a BISON-Dakota [34] framework was developed to optimize the FCCI correlation parameters using FIPD-based time-varying power, neutron flux and coolant mass flux rate as well as BISON's intrinsic coolant channel model. Here, the same framework was used to update the optimized FCCI correlation parameters using the new FIPD-based time-varying temperature boundary conditions.

The FCCI wastage thickness predicted by the new correlation parameters and FIPD-based temperature boundary condition is compared with the results based on the BISON coolant channel models in Figure 3-5. By using the FIPD-based temperature boundary condition, pin-by-pin difference is much more prominent compared to the original coolant channel approaches. To be specific, fuel pin DP04, DP70, and DP11, which were located away from dummy pins and close to reconstituted pins (i.e., DP57, DP71, DP80 and DP83), are predicted to form thicker FCCI wastage layer than other U-10Zr/HT9 pins. Additionally, as discussed in Section 2.4, the new FIPD-based temperature boundary condition approach leads to FCCI wastage thickness prediction like the results using the generic coolant channel model for fuel pins located in the outer regions. For the pins in the inner region, the wastage thickness predicted by the new method is closer to the results using the sodium coolant channel model instead. All these differences are reasonable given the pin-by-pin temperature difference provided by the FIPD-based boundary condition.

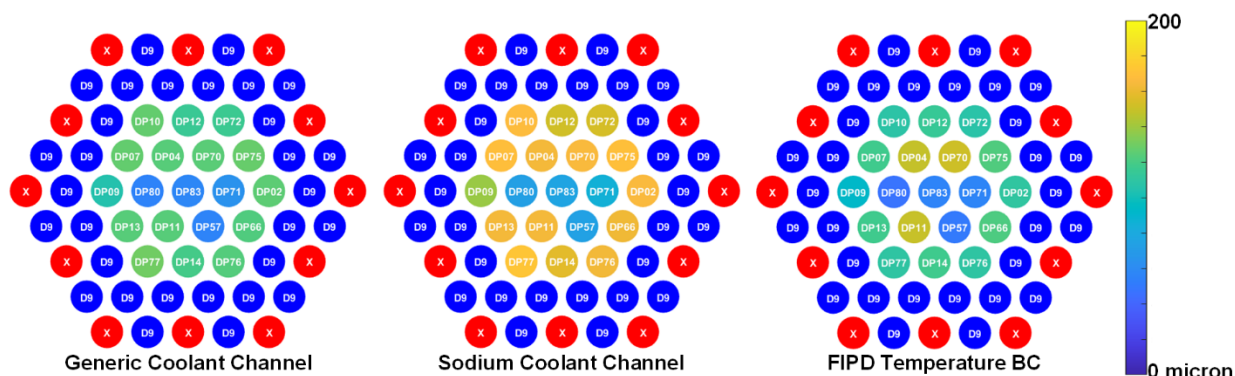


Figure 3-5 Maximum FCCI wastage thickness of X447A pins as predicted by BISON using the FIPD-based temperature BC in comparison with the results using BISON's generic and sodium coolant channel models.

The maximum CDFs of pins irradiated in X447A predicted by the new FIPD-based temperature boundary condition are also illustrated in Figure 3-6. Determined by the temperature difference mentioned above, pins DP04, DP11 and DP70 have CDF > 0.5 and DP75 also have a relatively high CDF. This observation is consistent with the fact that pins DP70 and DP75 failed during the experiment and that pins DP04 and DP11 were regarded as the sibling surviving pins of the two failed pins. For all the other U-10Zr/HT9 pins irradiated in X447/A experiment, the predicted CDFs are around 0.1 or lower, leading to low failure probability.

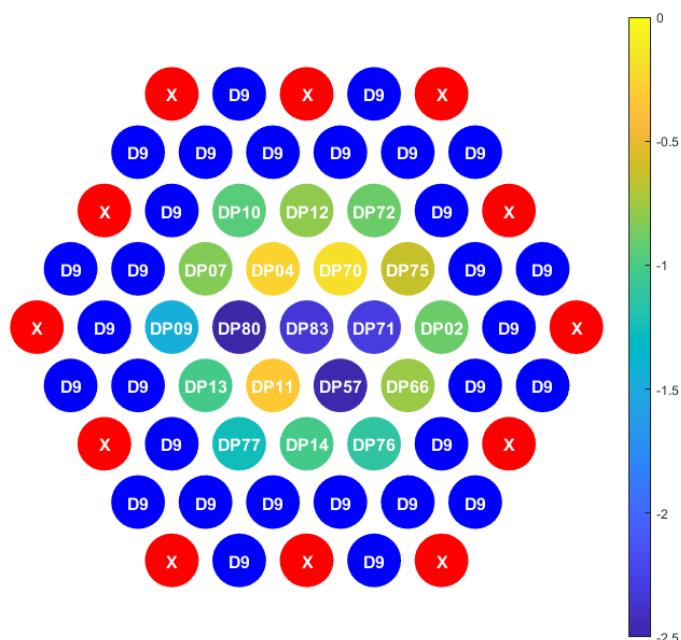


Figure 3-6 Pin-by-pin logarithmic CDF as predicted by BISON using the FIPD-based temperature BC.

Based on the pin-by-pin CDF predicted by the new temperature boundary condition approach, the probabilities of observing different numbers of failed pins were also updated and are compared with the results from the original approaches in Figure 3-7. The new approach leads to a cladding failure scenario in between the generic coolant channel and sodium coolant channel results, which is consistent with the previous speculation.

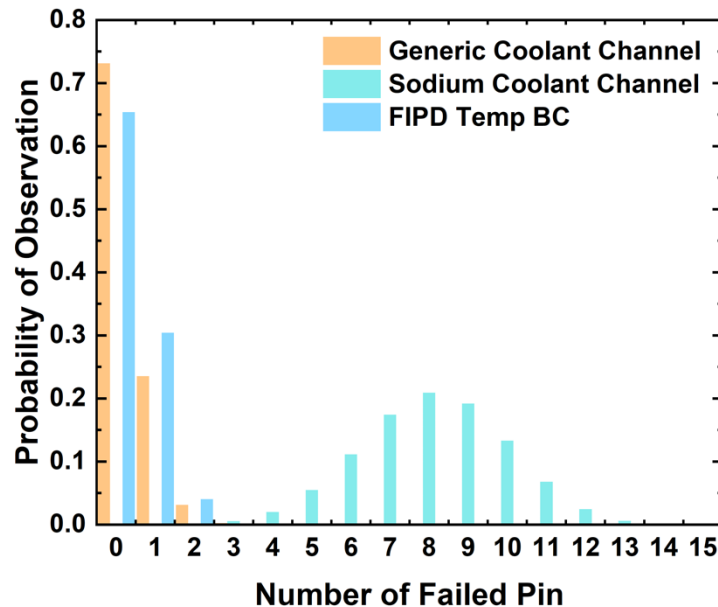


Figure 3-7 The probability of observing a specific number of failed pin as predicted by BISON using different temperature BCs.

4 Assessment of Low-Burnup Swelling

Metallic fast reactor fuels U-10Zr and U-xPu-10Zr swell significantly due to accumulation of both solid and gaseous fission products [35]. As the fuel swelling behavior is directly related to other important fuel performance phenomena, such as fission gas release, thermal conductivity degradation, and eventually fuel-cladding mechanical interaction (FCMI), it is regarded as one of the most relevant fuel behaviors that need to be reliably predicted by fuel performance codes.

Metallic fuels swell rapidly in the very beginning of the irradiation. The volumetric gaseous swelling strain usually reaches ~33% within 2% atomic burnup and then stalls due to the initiation of significant fission gas release. On the other hand, the solid fission product swelling strain can be approximated as proportional to burnup (~1.5% per 1% atomic burnup). To accommodate the swollen fuel, metallic fuels are commonly designed with a relatively low smeared density, leaving a wide initial fuel-cladding gap thermally bonded by liquid sodium. It was found that an approximately 75% smeared density is needed to avert premature cladding failure due to rapidly swelling fuel slugs. Therefore, two major stages of swelling must be captured by the fuel performance code such as BISON: (1) the rapid swelling stage during the low burnup regime (<~2%) and (2) the slow swelling stage once the fuel-cladding gap is closed. Among these two stages, the low-burnup stage is especially important due to the involvement of complex microstructural procedures and kinetics and therefore needs comprehensive evaluation, improvements, and V&V efforts.

Additionally, some innovative reactor designs, including Oklo's Aurora microreactor, adopt low-burnup (<1%) and low-temperature metallic fuels [36]. Hence, establishing a working framework under BISON to systematically evaluate low-burnup metallic fuel swelling modeling performance by leveraging BISON-FIPD integration is crucial for promoting the application of BISON for commercial reactor design as well as fuel qualification/licensing activities.

4.1 Brief Review of Investigated BISON Swelling Model

A series of different swelling correlations have been implemented into BISON in the past few years. This includes the original BISON metallic fuel swelling correlation `UPuZrVolumetricSwellingEigenstrain` object developed by Medvedev, and the `ADUPuZrGaseousEigenstrain` object based on Olander's formula. Later, the LIFE-METAL fuel swelling correlation was also implemented into BISON as the `UPuZrVolumetricSwellingEigenstrainLM` object for reference (termed "LM" model from now on). Most recently, a set of parameters were also developed based on the new `ADSimpleFissionGasViscoplasticityStressUpdate` object for metallic fuels (termed "VP" model from now on). All these fuel swelling models are empirical at this stage so that more improvements are expected in the next few years to provide more accurate and predictive capabilities for metallic fuel swelling modeling by involving more microstructural information from lower-length-scale simulations. In this chapter, a BISON-FIPD based low-burnup swelling evaluation framework will be established and tested using the existing swelling models. It is worth mentioning that this framework will be useful for improving the current models' parameters and for evaluating future advanced swelling models as well. Here, only the LM and VP swelling models are focused on to provide examples of using this low-burnup swelling evaluation framework. The details of these swelling models can be found on BISON's documentation website.

4.2 IFR Irradiation Experiment X423 in FIPD

The IFR irradiation experiment X423 [37] was designed to investigate the low-burnup swelling behavior. It was the only metallic fuel irradiation experiment that provide PIE data before fuel-cladding gap closure. Therefore, the data of X423 maintained in FIPD are the key to establishing a BISON-FIPD integration enabled low-burnup metallic fuel swelling evaluation framework.

4.2.1 Brief Introduction of the X423 Experiment

The X423 experiment was performed at EBR-II to obtain irradiation experience with large-diameter fuel pins (0.223 inch diameter compared to 0.173 inch diameter) and various plutonium contents (0%, 3%, 8%, 19%, 22% and 26%). The uranium enrichment was also adjusted based on the Pu loading to ensure similar power for all the irradiated fuel pins. In order to enable examination of low-burnup behavior, during the target ~5% peak atomic burnup, three reconstitutions were performed to obtain PIE data at ~0.5%, ~1.0%, and ~2.0% peak atomic burnup. Divided by these reconstitutions, the experiment can be further divided into X423, X423A, X423B, and X423C.

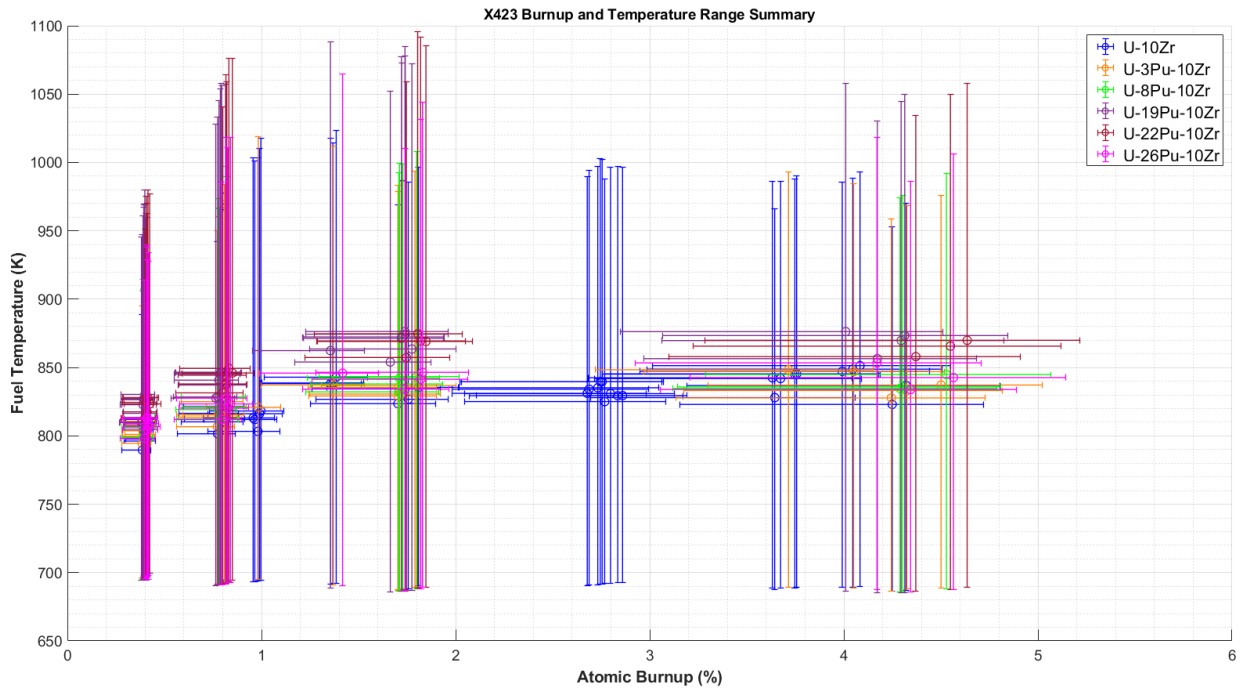


Figure 4-1 Summary of time-and-radial averaged axial fuel temperature range and burnup range of fuel pins with different Pu loading values that were irradiated and examined in the IFR experiment X423.

The X423 experiment adopted the D-37 type hardware, which contains 37 fuel pins with 0.290 inch cladding outer diameter (OD). Considering the three reconstitutions, there are 148 sets of irradiated pin data stored in FIPD for this experiment. A summary of the time-averaged fuel temperature and atomic burnup ranges of all the 147 fuel pins can be found in Figure 4-1. The time-and-radial averaged axial fuel temperature ranges from 700 K up to beyond 1000 K. More importantly, for U-10Zr binary fuel, X423 PIE data almost covers the entire low-burnup range from ~0.3% up to ~5%.

For Pu-containing fuel pins, the atomic burnup below ~2% is also well covered by the X423 experiment. Therefore, this experiment has its unique merits for fuel performance model evaluation, optimization and V&V efforts that are focused on low-burnup behaviors.

4.2.2 Leveraging BISON-FIPD Integration

4.2.2.1 Irradiation Condition Parameters in FIPD

FIPD contains a series of data that are essential for the establishment of this low-burnup swelling evaluation framework. Like the X447 related simulations, which are discussed early in this report, the FIPD-based data that are used as input for BISON simulations are listed in Table 4-1.

Table 4-1 FIPD-based input data used in the low-burnup swelling evaluation framework.

FIPD-Based Data	Related BISON/MOOSE Object
Fuel pin geometry parameters	FIPDRodletMeshGenerator
Time-varying pin-averaged power	PiecewiseLinear
Time-varying pin-averaged fast flux	PiecewiseLinear
Power peaking factor	FIPDAxialProfileFunction
Fast flux peaking factor	FIPDAxialProfileFunction
Time-varying cladding surface temperature	FIPDAxialProfileFunction

4.2.2.2 Post-Irradiation Examination Results in FIPD

Aside from the irradiation condition data, another section of data that are valuable for fuel performance model assessment are PIE results. FIPD contains a huge amount of PIE data collected using a series of different approaches. For example, in the FCCI/CCCI and cladding degradation model assessment, contact profilometry and laser profilometry data that provide the cladding deformation information are the key as shown in Section 2. Here, for low-burnup swelling model assessment, neutron radiography (NRAD) results are the most crucial data that provide fuel slug dimension information after irradiation.

All neutron radiography NRAD data stored in FIPD [17] were originally measured using the NRAD imaging facility established at the Hot Fuel Examination Facility (HFEF). At HFEF, both thermal neutrons (captured by dysprosium foils) and epithermal neutrons (captured by indium foils) are used for NRAD technology through an indirect imaging approach to prevent interference from gamma radiation. As the fissile materials in fuels have high thermal neutron adsorption cross sections, the thermal neutron NRAD imaging is a powerful tool to measure fuel dimensions without breaking the cladding. This non-destructive PIE method made it possible to measure the same fuel pin at different burnup points within the X423 experiment.

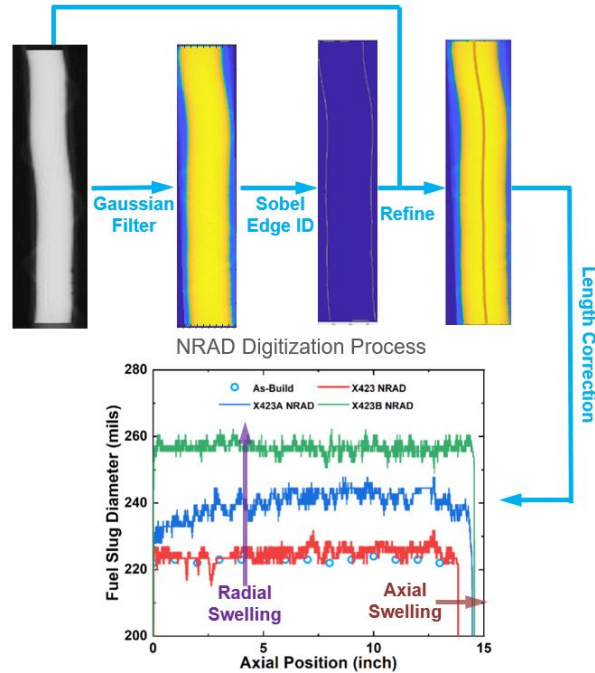


Figure 4-2 Procedures used to extract fuel radial and axial swelling strain from thermal neutron NRAD images.

The raw thermal neutron NRAD data are stored in FIPD as image files. In order to extract the fuel dimension information from these images, a series of image processing methods are utilized together. As shown in Figure 4-2, Gaussian filter is first used to smoothen the NRAD images so that the noise and bad pixels are eliminated. Then, Sobel edge identification algorithm is used to detect the fuel slug edge (assuming the fuel edge causes the major contrast gradient). Because some local details are also lost during Gaussian filtering, the neighboring pixels of the identified edges in the raw (before Gaussian filtering) NRAD image are revisited to ensure the local maximum contrast gradient positions so that the fuel edge positions are refined. As the fuel slug may be slightly bent, the length of the fuel is corrected based on the curvature profile of the fuel centerline defined by the two edges. Then, both radial and axial swelling of the fuel slug can be quantified from the NRAD image. These processed data are also available in FIPD. In this study, as the current fuel anisotropic swelling factor is a manually adjusted parameter for all existing metallic fuel swelling models, the evaluation is focused on the radial swelling.

4.2.2.3 Development of BISON Object to Facilitate PIE-Prediction Comparison

The axial PIE data in FIPD are usually downloadable as CSV files. In order to facilitate the direct use of these CSV files for BISON metallic fuel model evaluation, verification and validation, a BISON object needs to be developed. Given the nature of these axial PIE data, a VectorPostprocessors object named FIPDAxialPIEComparison was developed.

FIPDAxialPIEComparison is a customized version of the SideValueSampler VectorPostprocessor. This object extracts a BISON calculated Variable or AuxVariable (e.g., displacement in the radial direction) on a given boundary as an axial profile. Meanwhile, it reads

another version of axial profile directly from a CSV file available at the FIPD. The CSV file usually contains post irradiation examination data (e.g., diameter profile of fuel or cladding) that are related to the extracted BISON calculated variable.

After appropriate processing, the predicted axial profile originating from BISON simulation and the FIPD-based axial profile are compared with each other to help evaluate BISON's performance in predicting the fuel behavior quantified by the extracted variable. The comparison result is provided as the relative difference profile between the two sets of axial profiles.

In FIPD, the legacy axial PIE data are usually provided in English units. To be specific, the axial positions are provided as distance from fuel/cladding bottom in inches; and the diameters of the fuel/cladding are provided in mils. To directly compare the PIE data with BISON prediction, the units need to be converted and the positions need to be scaled and/or shifted based on the specific mesh parameters used by BISON. Thus, this `FIPDAxialPIEComparison` `VectorPostprocessor` must be used along with `FIPDRodletMeshGenerator` so that essential mesh geometry parameters can be obtained through `MeshMetaDataInterface`. Considering the different geometry features between fuel and cladding, users can set `involved_component` as either `fuel` or `cladding` to use the corresponding `MeshMetaData`.

If this object is applied to a `fuel` component, the axial positions read from the CSV file are first converted into the fractional form y/L , where y is the distance from fuel bottom and L is fuel length. The fractional axial positions are then converted back to the corresponding absolute form using the `MeshMetaData`. On the other hand, if this object is applied to a `cladding` component, the axial positions directly inherit the input values (after proper unit conversion). The zero axial position of the cladding is regarded as the bottom of the fuel slug position by default. Users may also use `axial_shift` to align the FIPD PIE data with the BISON mesh.

A common application of this object is to compare the BISON-predicted radial displacement of metallic fuel slug or cladding of an EBR-II irradiated fuel pin with the corresponding PIE data available in FIPD to facilitate BISON metallic fuel model evaluation, verification, and validation (V&V). All the PIE measurements available in FIPD were made at ambient temperature after irradiation. However, the BISON calculated displacement variable also contains the contribution from thermal expansion. Therefore, the thermal expansion contributed radial displacement can be excluded by providing a thermal strain `AuxVariable` (i.e., `thermal_strain_variable`) that contains axial layered average thermal strain profile. Thus, the results can be directly compared with the PIE data.

In this low-burnup swelling model evaluation framework, the object was used to compare BISON predicted fuel diameters with NRAD-deduced fuel diameters to provide a direct criterion for swelling model evaluation.

4.3 Assessment Results

After applying the aforementioned BISON-FIPD integration approaches, all the fuel pins that were irradiated in the IFR experiment X423 were simulated using BISON. For each pin, a 150 (axial) \times 10 (radial)-QUAD4-element RZ axisymmetric mesh was used for the fuel slug at this stage. The

fuel diameter evolution at all the quadrature points on the outer surface is compared with the PIE data using the FIPDaxialPIEComparison object. A summary of this comparison can be found in Figure 4-3.

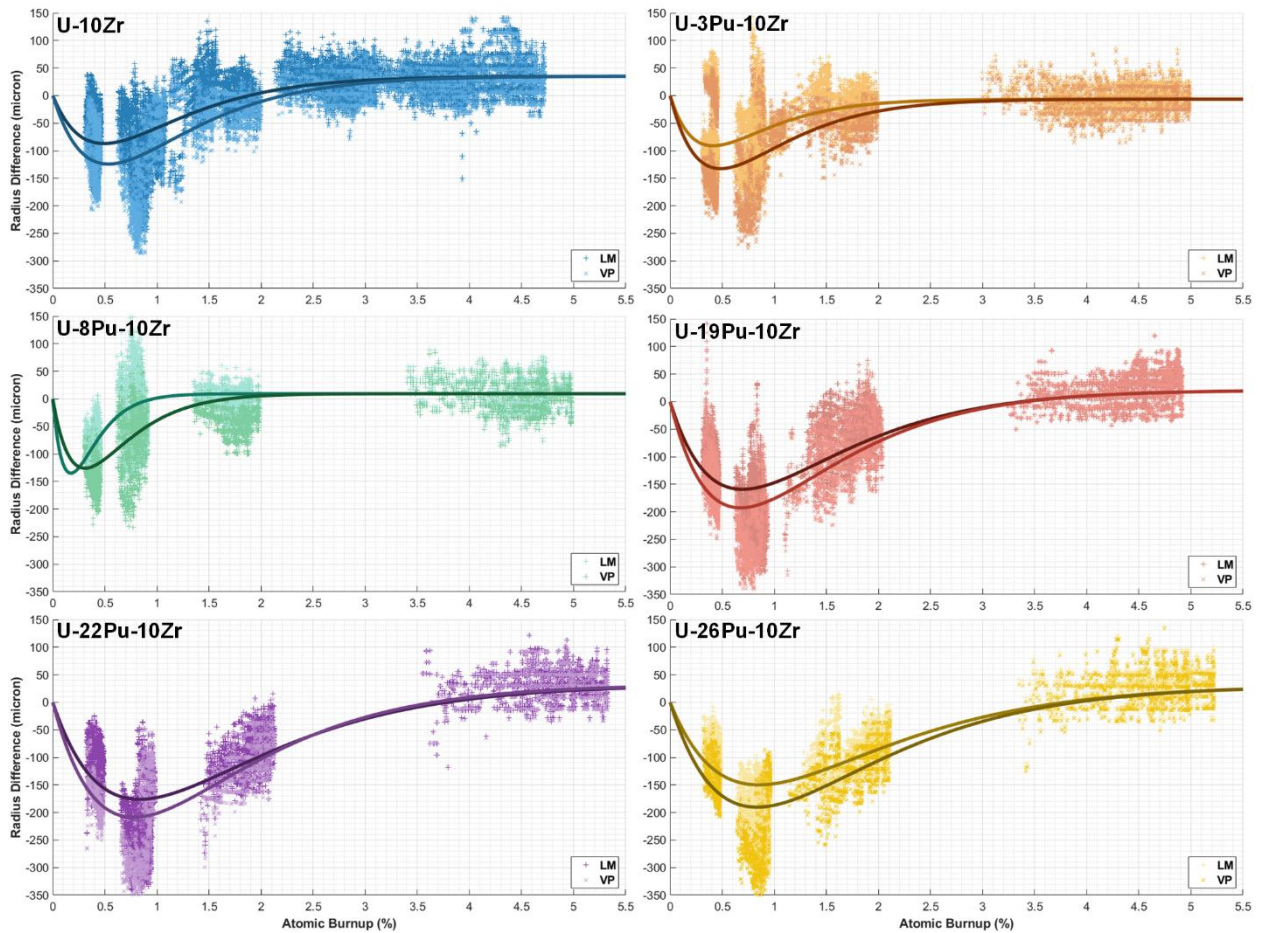


Figure 4-3 Differences between BISON predicted fuel radii using the two current swelling models and NRAD measured fuel radii as a function of burnup.

Using both LM and VP swelling models, BISON is capable of predicting the gap closure event when the atomic burnup exceeds approximately 2~2.5% atomic burnup depending on the Pu content. That means the swelling models are quite reliable for any intermediate and high burnup simulations of metallic fuels. On the other hand, before the gap closure event, the difference between BISON predicted radius and the PIE measured radius is always negative. Namely, both LM and VP models slightly overestimate the swelling rate at low burnup. Therefore, the current BISON swelling models can provide conservative approximations at low burnup, while further improvements can be made to reduce this overestimate to enable high-fidelity swelling estimation, especially for those fuels that are designed to mainly operate at low burnup.

More details about the comparison between BISON prediction and PIE data can be found in Figure 4-4 through Figure 4-9. Combined with the Figure 4-3, the overestimation of the fuel radius at lower burnup seems more significant for high-Pu-loading ternary fuel. Therefore, a Pu-dependent

swelling model may be needed to capture this behavior. It is worth mentioning that the general U-Pu-Zr swelling parameters set was used here for the LM model. The LM model also provides specified parameters sets for U-10Zr and U-19Pu-10Zr, which may be explored in future. Also, it is noticeable that for almost all the fuel pins at 0.5% atomic burnup, the PIE measured fuel radius is almost the same as the as-fabricated radius. Hence, it seems that the fuel swelling kinetics of metallic fuel is slow at the very-low burnup and becomes rapid between 0.5% and 1.0% atomic burnup. This observation may imply some key microstructural mechanism of fuel swelling that needs to be captured by the advanced metallic fuel swelling models. This phenomenon may also be important for the accurate fuel performance predictions for those low-burnup fuel designs (e.g., Oklo).

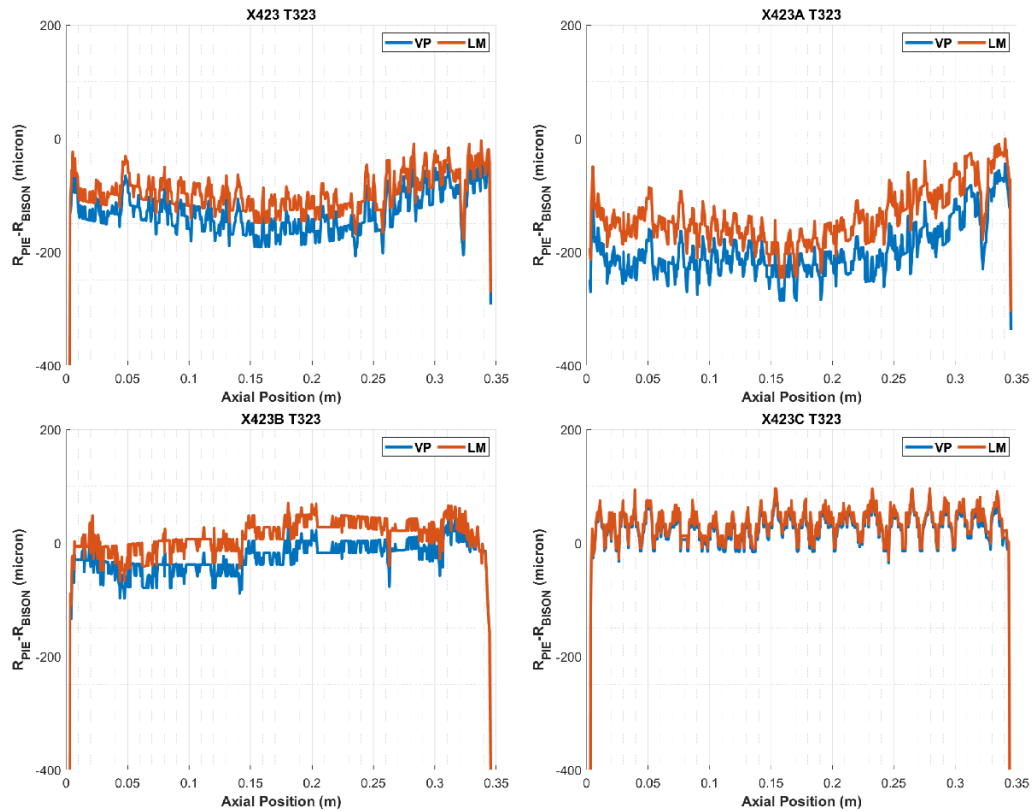


Figure 4-4 Comparison between BISON predicted fuel radius and NRAD measured fuel radius for a typical U-10Zr pin.

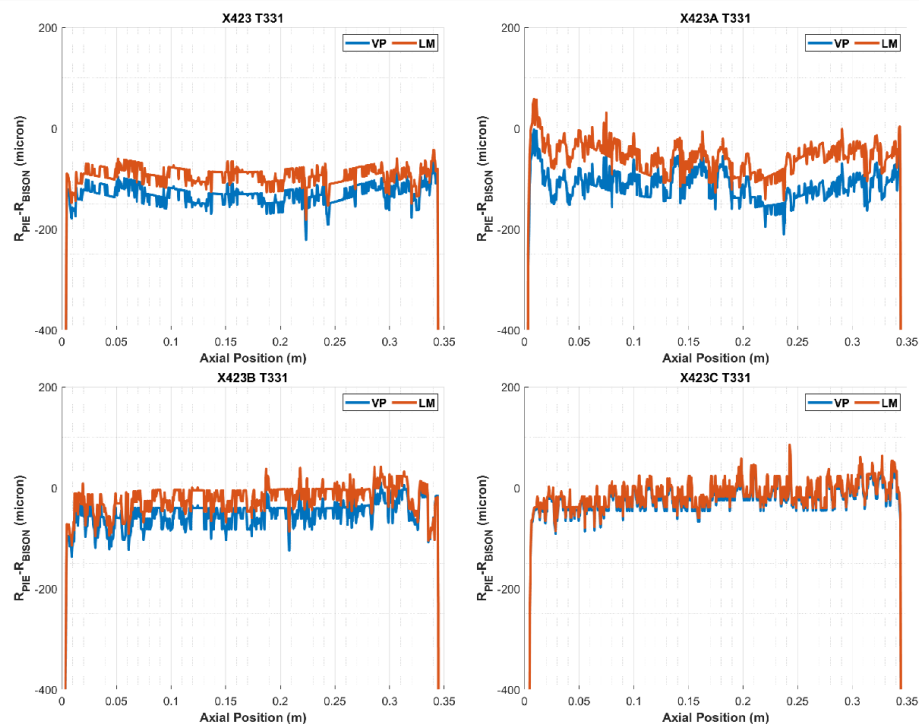


Figure 4-5 Comparison between BISON predicted fuel radius and NRAD measured fuel radius for a typical U-3Pu-10Zr pin.

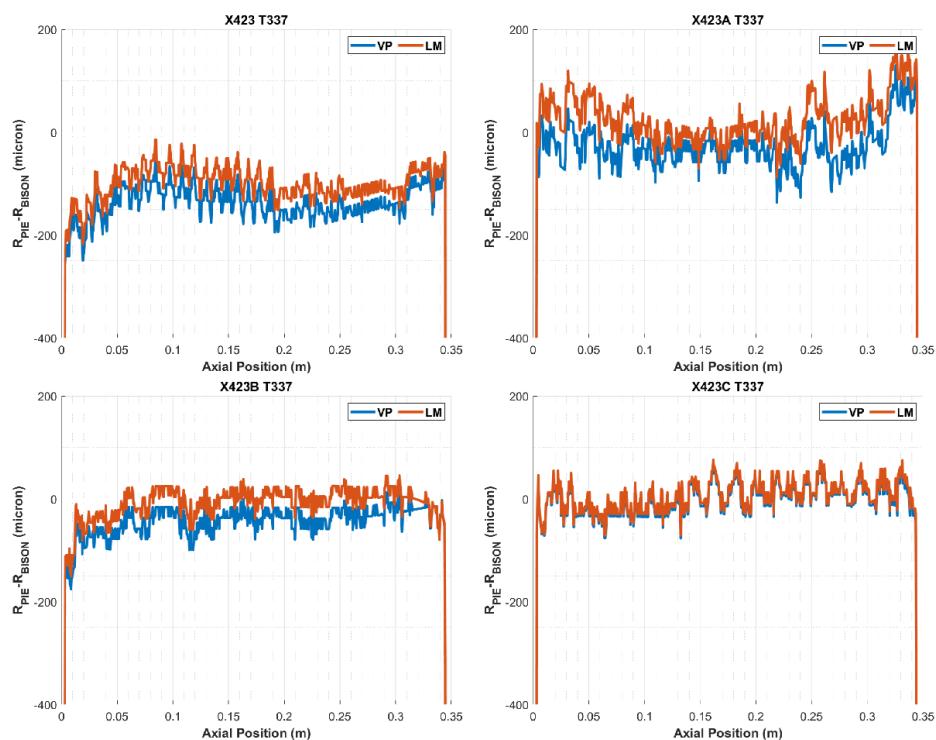


Figure 4-6 Comparison between BISON predicted fuel radius and NRAD measured fuel radius for a typical U-8Pu-10Zr pin.

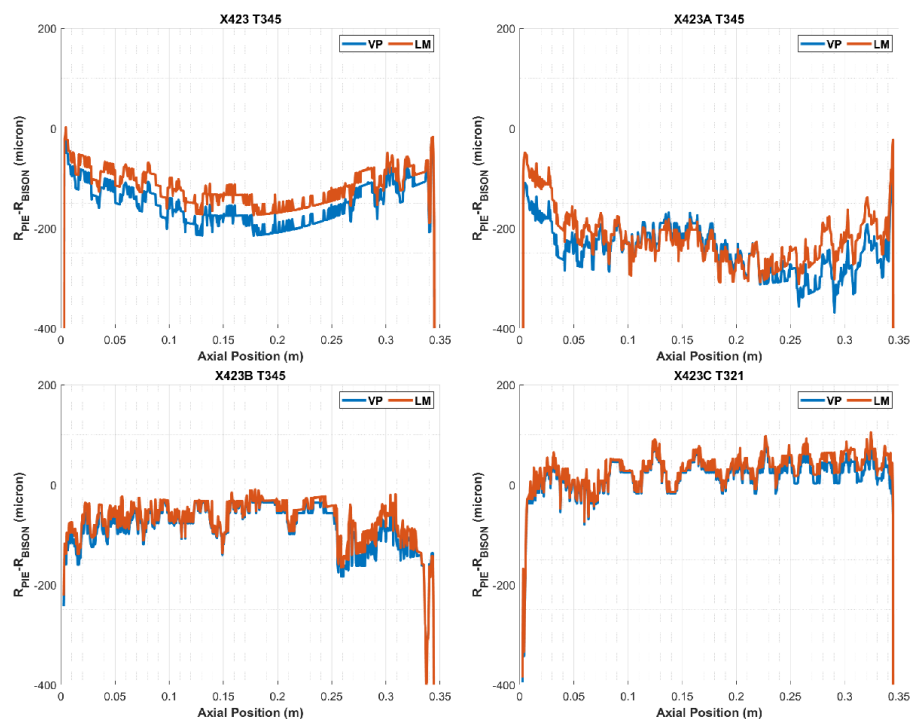


Figure 4-7 Comparison between BISON predicted fuel radius and NRAD measured fuel radius for a typical U-19Pu-10Zr pin.

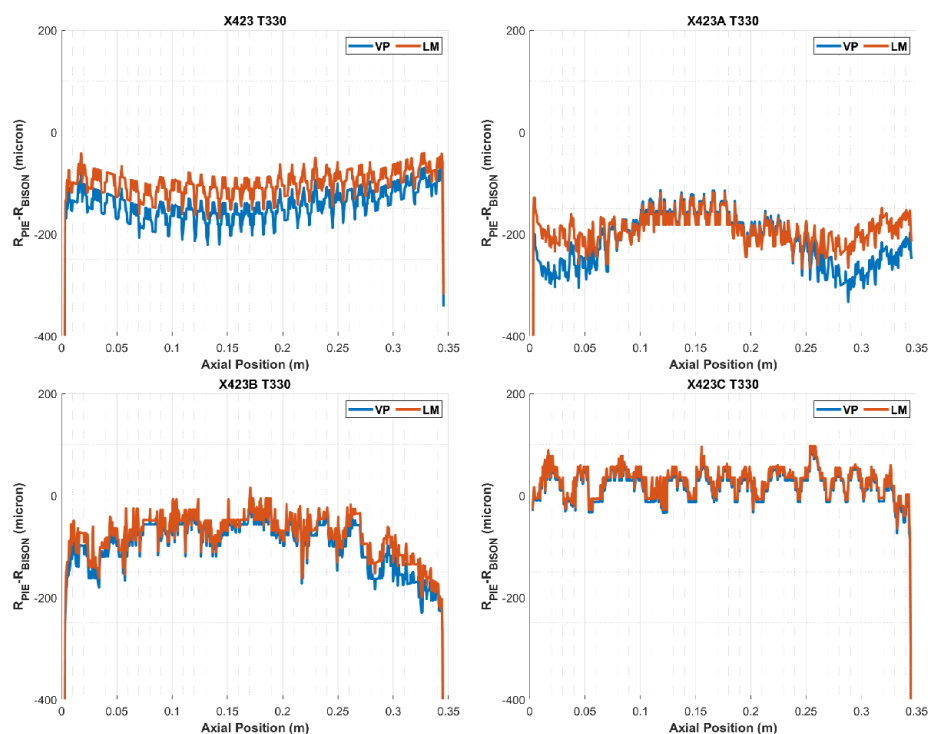


Figure 4-8 Comparison between BISON predicted fuel radius and NRAD measured fuel radius for a typical U-22Pu-10Zr pin.

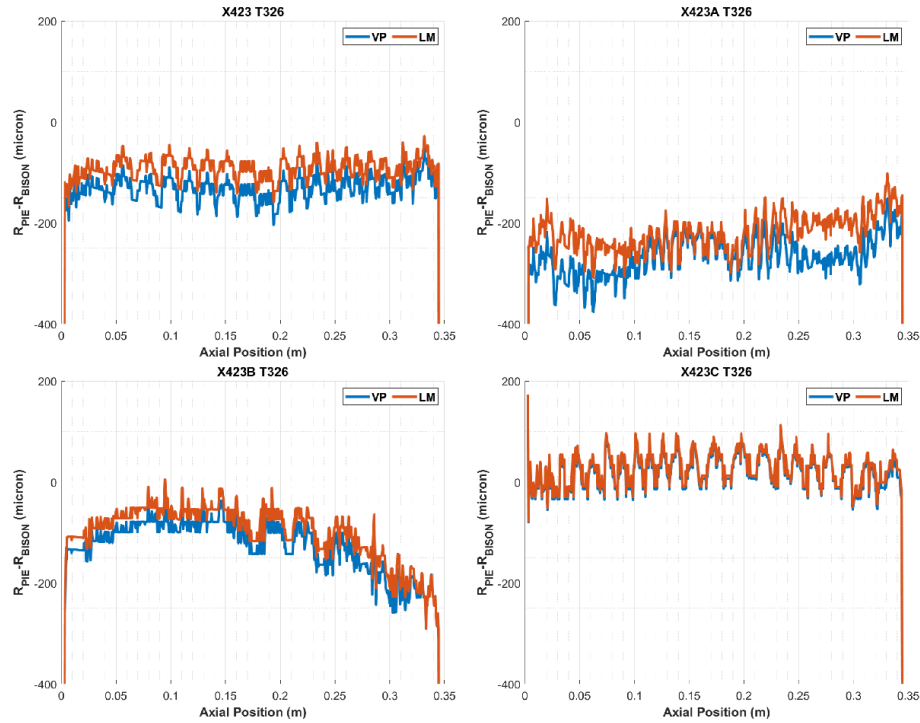


Figure 4-9 Comparison between BISON predicted fuel radius and NRAD measured fuel radius for a typical U-26Pu-10Zr pin.

The scalar average differences in fuel radius between BISON simulation and the PIE NRAD data can also be calculated for all the fuel pins irradiated in the X423 experiment. This style of quantitative data can be a good criterion to evaluate the performance of metallic fuel swelling models.

Again, it is worth mentioning that the axial growth of the fuel was not focused here as all the current models require a manual input for swelling anisotropy. In the NRAD data, the fuel axial growth information is also included. Therefore, axial growth feature will be added as a future update to enable evaluation of advanced fuel swelling models that can intrinsically capture the anisotropic swelling behavior.

5 Conclusions and Future Plans

5.1 Conclusions

In FY2021, a series of achievements have been made at Argonne to contribute to the BISON metallic fuel development as well as V&V activities.

A cladding mechanical property degradation model based on FCCI/CCCI wastage calculations was developed, optimized, and implemented into the BISON fuel performance code. The combination of both implemented FCCI/CCCI correlations and cladding degradation model was evaluated using IFR X447/A experiment data which are benefiting from ongoing BISON-FIPD integration efforts. With these approaches, BISON's capabilities of predicting fuel cladding damage and deformation that are consistent with PIE results are significantly improved.

During the cladding degradation evaluation, it was found that current BISON's coolant channel models limit the code's performance in predicting fuel pin's behavior when adjacent pins have dissimilar power. This limitation can be eliminated by expanding the BISON-FIPD integration framework. In FY2021, time-varying cladding outer surface temperature profile data were developed and made available to FIPD users. A new BISON object was also developed to directly use such data files from FIPD as temperature boundary conditions. The new approach was evaluated and proved to provide improved pin-by-pin temperature and fuel performance prediction for the IFR experiment X447.

To better evaluate, verify and validate current and future low-burnup swelling models, a BISON-FIPD-integration-enabled evaluation framework was developed. A new VectorPostprocessor object was implemented to enable direct comparison between BISON predicted axial profiles and PIE axial profiles available in FIPD. With this new feature, the low-burnup swelling model evaluation framework was established based on the comprehensive fuel swelling data from the IFR experiment X423. The current BISON metallic fuel swelling models were found accurate for intermediate and high burnup swelling predictions. For low burnup (<2.5% atomic burnup), current models overestimate the swelling rate and thus provide conservative results. Future efforts need to be made to further improve the low-burnup performance of the swelling models so as to enable high-fidelity fuel performance simulations using BISON, especially for those innovative low-burnup fuel designs. The developed evaluation framework can also be expanded to other model evaluation such as cladding creep and FCCI/CCCI models using profilometry data as well as burnup models using gamma scanning data available in FIPD.

5.2 Future Plans

In FY2022, multiple activities can be continued or initiated based on the achievements made in FY2021.

The metallic fuel assessment cases have been continuously improved by leveraging BISON-FIPD integration. An FIPD action is being developed for BISON to wrap up all BISON-FIPD integration tools into a single input block to improve users' experience in FIPD-powered BISON metallic fuel models V&V. The BISON-FIPD integration and FIPD Action will be further improved by enhanced integration and additional BISON objects in FY2022. As the BISON metallic fuel

assessment cases based on FIPD will keep expanding in the next few FYs (e.g., X441, X447 and X423, etc.), a systematic mechanism will need to be established to help those BISON users who have access to FIPD get FIPD data files to run BISON assessment cases. A Gitlab repository that contains FIPD data files needed by BISON assessment case may be created and will work as a BISON submodule in the future.

Out-of-pile transient experiments are another batch of the IFR experiments that will be essential for BISON metallic fuel V&V efforts, which are maintained in Argonne's OPTD database [38]–[40]. Those FBTA (Fuel Behavior Test Apparatus) and WPF (Whole Pin Furnace) experiments provides experimental data with precisely controlled and measured conditions (compared to in-pile experiments) for transient scenarios. These out-of-pile transient experiments, along with in-pile transient experiments (e.g., M-series experiments in TREAT [41]), will be important to BISON metallic fuel V&V in addition to the currently focused steady state experiments. Efforts can be initiated to investigate the approaches to utilize these legacy data to evaluate BISON models performance during transient scenarios.

Additionally, the low-burnup swelling model evaluation framework developed in FY2021 has been focused on radial swelling. More efforts will need to be made to implement axial fuel growth and anisotropic growth into the framework. Other minor improvements may also be made in FY2022. For example, other FIPD-based information, such as pin-by-pin burnup profile, can be used with the BISON burnup object to provide burnup information with higher accuracy.

REFERENCES

- [1] T. Sofu, “A review of inherent safety characteristics of metal alloy sodium-cooled fast reactor fuel against postulated accidents,” *Nucl. Eng. Technol.*, vol. 47, no. 3, pp. 227–239, 2015.
- [2] D. C. Crawford, D. L. Porter, and S. L. Hayes, “Fuels for sodium-cooled fast reactors: US perspective,” *J. Nucl. Mater.*, vol. 371, no. 1–3, pp. 202–231, 2007.
- [3] D. C. Crawford, S. L. Hayes, and J. J. Powers, “VTR Startup Fuel Paper for NFSM ”, INL/EXT-18-44673, 2018.
- [4] A. M. Yacout and M. C. Billone, “Pre-Licensing Evaluation of Legacy SFR Metallic Fuel Data”, ANL-ART-76, 2016.
- [5] S. Hayes, D. Dempsey, J. M. Harp, and G. L. Povirk, “Developmental Objectives for Advanced Reactor Fuels”, INL/EXT-16-39923, 2017.
- [6] W. J. Carmack, S. L. Hayes, J. M. Harp, R. S. Fielding, S. A. Maloy, and T. A. Saleh, “Overview of the US DOE fast reactor fuel development program”, INL/CON-16-40021, 2017.
- [7] A. M. Yacout, “Long-Life Metallic Fuel for the Super Safe, Small and Simple (4S) Reactor”, AFT-2008-000056, 2008.
- [8] R. L. Williamson *et al.*, “Multidimensional multiphysics simulation of nuclear fuel behavior,” *J. Nucl. Mater.*, vol. 423, no. 1–3, pp. 149–163, 2012.
- [9] D. Gaston, C. Newman, G. Hansen, and D. Lebrun-Grandie, “MOOSE: A parallel computational framework for coupled systems of nonlinear equations,” *Nucl. Eng. Des.*, vol. 239, no. 10, pp. 1768–1778, 2009.
- [10] R. L. Williamson *et al.*, “Validating the BISON fuel performance code to integral LWR experiments,” *Nucl. Eng. Des.*, vol. 301, pp. 232–244, 2016.
- [11] K. A. Gamble, G. Pastore, D. Andersson, and M. W. D Cooper, “BISON capability and validation for U₃Si₂, Cr₂O₃-doped UO₂, FeCrAl, and Cr-coated Zircaloy ATF concepts ”, INL/CON-20-57530, 2020.
- [12] J. D. Hales, R. L. Williamson, S. R. Novascone, D. M. Perez, B. W. Spencer, and G. Pastore, “Multidimensional multiphysics simulation of TRISO particle fuel,” *J. Nucl. Mater.*, vol. 443, no. 1–3, pp. 531–543, 2013.
- [13] P. Medvedev, S. Hayes, S. Bays, S. Novascone, and L. Capriotti, “Testing fast reactor fuels in a thermal reactor,” *Nucl. Eng. Des.*, vol. 328, pp. 154–160, 2018.
- [14] J. Galloway, C. Unal, N. Carlson, D. Porter, and S. Hayes, “Modeling constituent redistribution in U--Pu--Zr metallic fuel using the advanced fuel performance code BISON,” *Nucl. Eng. Des.*, vol. 286, pp. 1–17, 2015.
- [15] Y. Miao, N. Stauff, A. Oaks, A. M. Yacout, and T. K. Kim, “Fuel performance evaluation of annular metallic fuels for an advanced fast reactor concept,” *Nucl. Eng. Des.*, vol. 352, p. 110157, 2019.
- [16] S. Novascone, P. Medvedev, J. W. Peterson, Y. Zhang, and J. Hales, “Modeling porosity

- migration in LWR and fast reactor MOX fuel using the finite element method,” *J. Nucl. Mater.*, vol. 508, pp. 226–236, 2018.
- [17] A. M. Yacout, A. Oaks, W. Mohamed, and K. Mo, “FIPD: EBR-II Fuels Irradiation & Physics Database”, ANL-ART-124, 2017.
 - [18] A. M. Yacout, K. Mo, A. Oaks, Y. Miao, T. Sofu, and W. Mohamed, “FIPD: The SFR metallic fuels irradiation & physics database,” *Nucl. Eng. Des.*, vol. 380, p. 111225, 2021.
 - [19] R. G. Pahl, C. E. Lahm, and S. L. Hayes, “Performance of HT9 clad metallic fuel at high temperature,” *J. Nucl. Mater.*, vol. 204, pp. 141–147, 1993.
 - [20] “BISON Documentation Website.” <https://mooseframework.inl.gov/bison/>.
 - [21] W. Jiang, B. W. Spencer, and J. E. Dolbow, “Ceramic nuclear fuel fracture modeling with the extended finite element method,” *Eng. Fract. Mech.*, vol. 223, p. 106713, 2020.
 - [22] M. C. M. Kazimi, “Heat Transfer Correlation for Analysis of CRBRP Assemblies,” 1976.
 - [23] G. J. Calamai *et al.*, “Steady State Thermal and Hydraulic Characteristics of the FFTF Fuel Assemblies,” *FRT-1582*, June, 1974.
 - [24] V. M. Borishanskii, M. A. Gotovskii, and E. V. Firsova, “Heat transfer to liquid metals in longitudinally wetted bundles of rods,” *Sov. At. Energy*, vol. 27, no. 6, pp. 1347–1350, 1969.
 - [25] K. L. Basehore and N. E. Todreas, “SUPERENERGY-2: a multiassembly, steady-state computer code for LMFBR core thermal-hydraulic analysis,” 1980.
 - [26] W. S. Yang and A. M. Yacout, “Assessment of the SE2-ANL Code using EBR-II Temperature measurements,” 1995.
 - [27] D. L. Porter, B. D. Miller, B. A. Hilton, and M. M. Jones, “HT9 swelling in high burnup fast reactor fuel pin components,” *J. Nucl. Mater.*, vol. 519, pp. 205–216, 2019.
 - [28] T. Ogata and T. Yokoo, “Development and validation of ALFUS: an irradiation behavior analysis code for metallic fast reactor fuels,” *Nucl. Technol.*, vol. 128, no. 1, pp. 113–123, 1999.
 - [29] A. M. Yacout and M. C. Billone, “Current Status of the LIFE Fast Reactors Fuel Performance Codes,” 2015.
 - [30] C. Nam, W. Hwang, and D.-S. Sohn, “Statistical failure analysis of metallic U-10Zr/HT9 fast reactor fuel pin by considering the Weibull distribution and cumulative damage fraction,” *Ann. Nucl. Energy*, vol. 25, no. 17, pp. 1441–1453, 1998.
 - [31] L. L. Briggs *et al.*, “Safety Analysis and Technical Basis for Establishing an Interim Burnup Limit for Mark-V and Mark-VA Fuel Subassemblies in EBR-II,” 2018.
 - [32] W. J. Carmack, “Temperature and burnup correlated FCCI in U-10Zr metallic fuel,” 2012.
 - [33] M. A. Smith, “Personal Communication.” 2020.
 - [34] B. M. Adams *et al.*, “DAKOTA, a multilevel parallel object-oriented framework for design optimization, parameter estimation, uncertainty quantification, and sensitivity analysis: version 5.0 user’s manual,” *Sandia Natl. Lab. Tech. Rep. SAND2010-2183*, 2009.

- [35] G. L. Hofman, R. G. Pahl, C. E. Lahm, and D. L. Porter, “Swelling behavior of U-Pu-Zr fuel,” *Metall. Trans. A*, vol. 21, no. 2, pp. 517–528, 1990.
- [36] “Combined License Application Documents for Aurora – Oklo Power Plant Application.” <https://www.nrc.gov/reactors/new-reactors/col/aurora-oklo/documents.html>.
- [37] R. G. Pahl, D. L. Porter, C. E. Lahm, and G. L. Hofman, “Experimental studies of U-Pu-Zr fast reactor fuel pins in the experimental breeder reactor-II,” *Metall. Trans. A*, vol. 21, no. 7, pp. 1863–1870, 1990.
- [38] C. Tomchik and A. Oaks, “OPTD: Out-of-Pile Transient Database”, ANL-ART-149, 2018.
- [39] C. Tomchik and A. Oaks, “Status and Availability of OPTD, the Out-of-Pile Transient Database”, ANL-ART-214, 2020.
- [40] C. Tomchik, “Out-of-Pile Furnace Tests on Fast Reactor Metallic Fuels Conducted at the AGHCF”, ANL-ART-217, 2021.
- [41] T. H. Bauer, W. R. Robinson, J. W. Holland, E. A. Rhodes, and A. E. Wright, “First overpower tests of metallic IFR [Integral Fast Reactor] fuel in TREAT [Transient Reactor Test Facility]: Data and analysis from tests M5, M6, and M7”, ANL-IFR-124, 1989.



Chemical & Fuel Cycle Technologies Division

Argonne National Laboratory
9700 South Cass Avenue, Bldg. 205
Argonne, IL 60439

www.anl.gov



Argonne National Laboratory is a U.S. Department of Energy
laboratory managed by UChicago Argonne, LLC